Universitat Politècnica de Catalunya
DEPARTAMENT DE TEORIA DEL SENYAL I COMUNICACIONS

MASTER'S THESIS

Study and Implementation of Estimation Algorithms of Time of Arrival and Received Signal Strength for the Localization of Mobile Terminals in Emergency Situations

Author:
Pere Joan GIMÉNEZ FEBRER

Advisor:
Alba PAGÈS-ZAMORA

October 2013

Contents

List of Figures

List of Tables

Chapter 1

Introduction

The work in this thesis has been conducted within the European research project RESCUECELL "Portable Kit For Detecting Trapped and Buried People in Ruins and Avalanches". The objective of this project is the development of a short range wireless network for the localization of mobile phones buried under ruins caused by disasters such as an earthquake. The system consists of a local GSM network to which mobile phones within the coverage area are forced to get connected and communicate, so that the information transmitted can be used for positioning purposes. Using localization procedures, an estimation of the mobile phone position can be obtained, and eventual victims trapped in the neighborhood of the phone can be rescued.

The RESCUECELL system is composed of one control center (CC) and a number of femtocell access points (FAPs). The CC is in charge of creating two networks: one to establish a communication link with the buried mobile terminals (MTs), and another to communicate with the FAPs. For a MT, the CC acts as a base transceiver station (BTS) from a standard GSM network so that the MT receives information in the downlink channel and transmits in the uplink channel. On the other hand, the FAPs communicate with the CC only, but are able to listen to the transmissions in the uplink channel, acting as sniffers. Fig. 1.1 shows a simplified scheme of the overall architecture of the RESCUECELL system.

Localization of a mobile device is usually performed in two steps. In the first step, the device exchanges Radio Frequency (RF) signals with a number of reference points for distance estimation. When the distance measurements to the reference points are available, a three-dimensional position estimate can be computed with a positioning algorithm. In the RESCUECELL system, the MT is forced to connect to the CC and transmit information so that the FAPs detect the signal in the uplink channel and perform several measurements. These measurements are the time of arrival (TOA) and the received signal strength (RSS) of the signal sent from the MT and detected at the FAPs. The TOA and RSS measurements are then forwarded to the CC, where a positioning algorithm is run to locate the MT.

The success of a rescue operation in hazard situations depends on a rapid and precise localization of the victims. The aim of the RESCUECELL network is therefore to perform

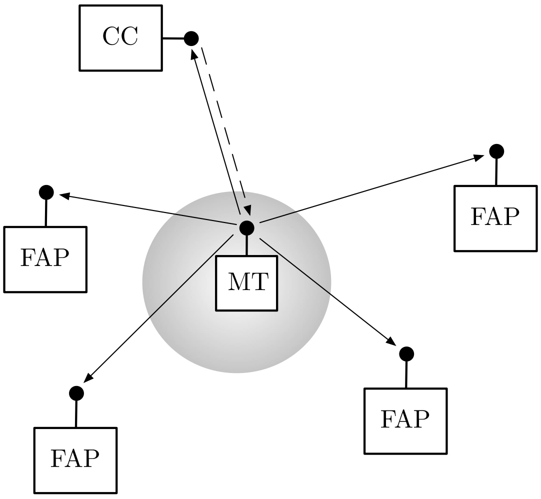

Figure 1.1: Architecture of the RESCUECELL system.

a fast and accurate localization of the MTs, so that eventual victims trapped or buried under the debris in the neighborhood of the MTs can be rescued as fast as possible.

An accurate measurement of the TOA and RSS is critical for a successful localization. Although the GSM protocol provides parameters that can be used to obtain the TOA and RSS, they cannot be used in the RESCUECELL system because of their low accuracy. Moreover, since GSM was not designed for the accurate positioning of mobile terminals, its specifications are a limiting factor for the measurement accuracy. Therefore, custom measurement procedures need to be implemented in the RESCUECELL system in order to achieve an accurate positioning.

The wireless channel in a disaster scenario poses additional challenges for the measurement of the localization parameters. Since the phone is buried under debris, the propagation path is blocked and the transmitted signals arrive at the FAPs with an additional delay and highly attenuated, which increases the measurement error. Furthermore, the signals are affected by multipath propagation due to the presence of multiple reflectors in the path between the MT and the FAP. The multipath propagation causes the reception of multiple copies of the transmitted signal, which also introduces an error in the parameter measurement.

Our objective in this work is to determine how accurately we would be able to estimate the TOA and the RSS in a real implementation of the RESCUECELL system. Hence, we propose several techniques to perform the estimations with improved accuracy. For the evaluation of the estimation techniques, a simulator of the communication link between the MT and one of the FAPs, referred thereafter as link simulator, has been implemented in MATLAB. The simulator has been built after the GSM specifications and it reproduces the transmission of information from the MT to the FAP and the posterior parameter estimation. In order to obtain accurate results, the link simulator incorporates a realistic model that accurately describes the propagation of a signal through the debris channel.

The contents of this thesis are organized as follows. Chapter 2 reviews the general characteristics of the GSM network and the current positioning methods available in GSM. Chapter 3 introduces the simulator of the GSM communication link. The principal components including the format of the transmission burst, the GMSK modulator, the realistic model of the debris channel, the receiver and the noise model are described in detail. Chapter 4 describes the proposed techniques for estimating the TOA and RSS, and the theoretical limits that will be used as a benchmark for the estimation performance. Chapter 5 presents the simulation results for the TOA and RSS estimation obtained in several configurations that reproduce both ideal and realistic scenarios. Finally, Chapter 6 summarizes the conclusions of this work.

Chapter 2

Mobile positioning in the GSM network

GSM is a standard for the second generation digital cellular networks used by mobile phones that was initially deployed in 1992. Although since its deployment GSM had the potential to provide localization information, it was the FCC E-911 ruling [1] issued in 1999 that motivated the development of positioning techniques in the GSM network [2]. This ruling required that by 2001 mobile operators had to be able to accurately locate the mobile phone users in their network. In the current standard, the 3GPP defines a series of location services and their performance requirements [3].

In this chapter, the general characteristics of the GSM900 network are briefly described, followed by an overview of several available positioning methods and their suitability for the RESCUECELL system.

2.1 GSM characteristics

The structure of a GSM network is shown in Figure 2.1. The area covered by a GSM network is divided into a number of cells. Each cell has its own base station, called base transceiver station (BTS), which facilitates wireless communication between the mobile terminals in the cell and the rest of the GSM network. Several BTSs are grouped together and controlled by a base station controller (BSC). In turn, the BSCs are controlled by the mobile switching center (MSC), which routes the communication between mobile terminals and connects to the public switched telephone network (PSTN) via the gateway MSC (GMSC).

Location services (LCS) are provided by a set of specialised nodes [4]. The gateway mobile location center (GMLC) receives location requests from a LCS client, coordinates the positioning process and returns the location estimate to the client. Connected to the GMLC, the home location register (HLR) provides information about the subscribers. The serving mobile location center (SMLC) calculates the position of the MT with the data obtained from the measurements performed by the location measurement unit (LMU). The LMU is usually attached to a BTS but it can also be used as a standalone node.

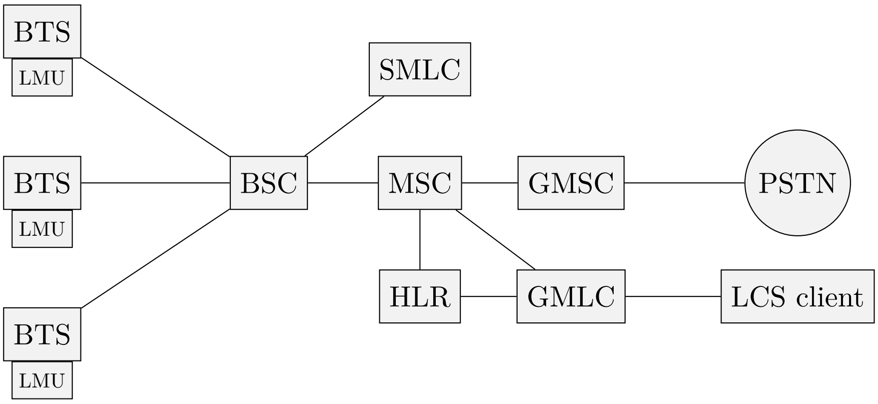

Figure 2.1: GSM network structure.

Depending on the chosen positioning technique, different algorithms and measurements can be used, providing estimations with varying degrees of accuracy.

GSM uses a combination of frequency division multiple access (FDMA) and time division multiple access (TDMA) as its medium access control protocol. In particular, the GSM900 frequency band is divided into two 25 MHz blocks: one for the uplink and one for the downlink. Each 25 MHz block is divided into 125 frequency channels of 200 kHz. TDMA is used in these channels, dividing the available transmission time into 8 slots, each with a duration of 577 μs. Blocks of 8 slots form a frame, and frames grouped together form multiframes and superframes. When a user wants to establish a call, he/she is assigned a frequency channel in the uplink and downlink, and a time slot in each frame for the duration of the call.

Tail	Data	S	Training sequence	S	Data	Tail
3	57	1	26	1	57	3

148 bits = $546.12\ \mu s$

Figure 2.2: Structure of a normal burst.

In GSM the information is transmitted over logical channels such as the broadcast control channel (BCCH) or the paging channel (PCH). A logical channel uses a number of slots in a superframe to transmit its data. In each slot, the data are transmitted in a burst modulated with the Gaussian minimum shift keying (GMSK) modulation. Although there are several types of bursts, the most commonly used is the normal burst, which has the format indicated in Fig. 2.2.

2.2 Available positioning methods in the GSM network

Thanks to the inclusion of nodes specially dedicated to positioning purposes and its cellular structure that covers large areas, the GSM network allows for the implementation of positioning techniques that locate the mobile terminals with different approaches. Typical geolocalization techniques such as angle of arrival (AOA), time of arrival (TOA), time difference of arrival (TDOA) and received signal strength (RSS) can be adapted and implemented in GSM networks. In these techniques, the deployed BTSs serve as the reference points where the parameters are measured by the LMU, while the SMLC performs all the calculations needed to localize the MT. In addition to these techniques, there are other methods specifically designed for cellular networks that can be used in GSM. These are cell-ID, enhanced observed time difference (E-OTD), RF fingerprinting and assisted GPS (A-GPS).

Cell-ID is the easiest location technique to implement since it takes advantage of the fact that the coverage area is already divided into cells. Each cell has its own unique identifier, called cell-ID, that can be used to position the MT. The BTS in each cell continuously broadcasts the cell-ID, which is received by all the MT in the area. If a MT knows its cell-ID and has knowledge about the structure and mapping of the network, it can assume that it is located inside the area covered by the cell. On the other hand, it is not always possible to locate the MT from the network side. The network only knows the cell-ID when the MT switches into dedicated mode [5], so it needs to communicate with the phone before attempting to locate it.

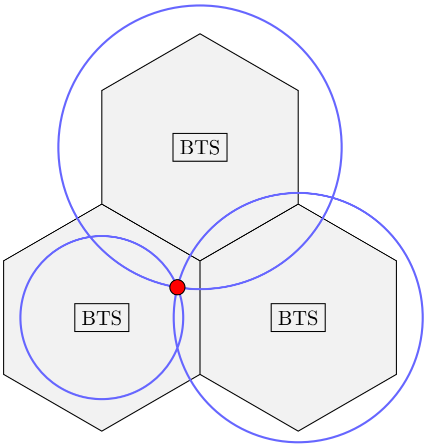

Figure 2.3: TOA location from three BTSs.

The TOA method computes the position of the MT using the signal propagation delay τ_0 between the MT and several BTSs. Usually, this method assumes the initial time of transmission to be known and requires perfect temporal synchronization between the MT and BTS. Each TOA measurement constrains the MT to a circle of radius $r = \tau_0 c$ m, where $c = 3 \cdot 10^8$ is the speed of light, around the BTS (Fig. 2.3), and the point where these circles intersect is the estimated position of the MT. Note that, as r scales with

c, the TOA measurements must be as accurate as possible because an error as small as 1 microsecond can result in a localization error of 300 meters. Also, synchronization between the BTS and the MT is crucial although it is hard to achieve because it does not only depend on the GSM network but also on the MT.

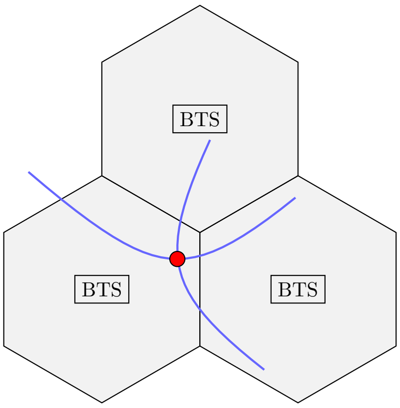

Figure 2.4: TDOA location from three BTSs.

The TDOA technique uses the difference of signal propagation delays between BTSs in pairs. Each TDOA measurement yields a hyperbolic curve on which the MT may be located. The intersection of two or more curves defines the estimated location of the MT as Figure 2.4 indicates. TDOA improves upon TOA in that there is no need for synchronization between the BTSs and the MT, although synchronization between BTSs is required. Given that the BTSs are all synchronized listening to the signal sent by the MT, the BTS-MT synchronization error is the same for all the BTSs and thus it is eliminated when the propagation delay differences are calculated.

The E-OTD approach is similar to TDOA, except that the measurements are performed at the MT. The MT listens to the broadcast channel of two neighbour cells and measures the time difference between the arrivals of the bursts. This requires the broadcast channels from the different BTSs to be synchronized, which can be achieved by deploying LMUs that listen to the BTSs transmissions and measure their timing offset. As in TDOA, two or more OTD measurements generate hyperbolic curves that mark the MT position at their intersection point. Although the positioning calculations don't need to be performed at the MT, there is legacy equipment that doesn't support OTD measurements. Another issue is that the MT may have difficulties listening to broadcast channels from distant cells in areas with low cell density.

The AOA method relies on triangulation to locate the MT. Each BTS equipped with an antenna array is able to determine the direction of propagation of the signal transmitted by the MT, resulting in a set of lines along which the MT can be located. The intersection point of the lines is the estimated MT position (Fig. 2.5). The performance of this method is severely affected by non-line-of-sight (NLOS) propagation because the signals arrive from multiple paths at random angles, which hinders the detection of the direction of propagation.

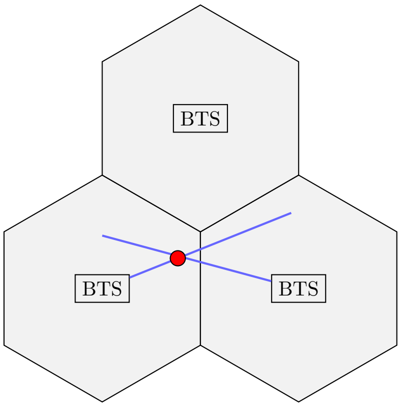

Figure 2.5: AOA location from two BTSs.

In the received signal strength indication (RSSI) technique, the MT measures the strength of the signals transmitted by neighbour stations and sends the measurements to the GSM network. Using an adequate path loss model, the RSS can be turned into a distance measurement that locates the MT on a circle around the BTS, and the intersection of three or more circles provides the position estimate. The RSS usually is not a reliable parameter because it is heavily affected by multipath propagation and shadowing from the environment. Besides, an extremely accurate path loss model is needed to precisely convert power measurements into distances.

The RF fingerprinting method uses the unique features that characterize a transmission in a determined area. The mobile operator records the signal features, such as power delay profile or RSS, at each position in the coverage area and stores them in a database. When a MT needs to be located, its fingerprint is compared to the ones in the database and the location with the matching fingerprint is set as the MT position. This technique requires databases with large amounts of data for accurate positioning.

If the MT is equipped with a GPS, the A-GPS method can be used to improve its time to first fix (TTFF). The TTFF is the time required for a GPS to identify at least four satellites and acquire their orbit data, a process that can take up to 15 minutes. A BTS with a GPS module can help reduce the TTFF by sending the satellite information to the MT over a data connection. This is a very efficient method since GPS provides highly accurate positioning and the amount of processing performed by the GSM network is minimal. However, it needs direct sky visibility and relies on equipment and software that not every MT may have.

2.3 Suitability of the GSM positioning methods in RESCUECELL

Given that the RESCUECELL system is based on GSM, the described positioning methods can be adapted and implemented. However, not all the methods are suitable for positioning a MT in an emergency situation because they do not provide enough accuracy or might not be compatible with all the MTs.

Technique	Measurement	Accuracy
Cell-ID	Cell identificator	Depends on cell size
TOA	Propagation delay	Medium-high
TDOA	Difference of propagation delays	Medium-high
E-OTD	Difference of arrival times	Medium-high
AOA	Angles	Medium-high
RSSI	Signal strength	Low
RF fingerprinting	Signal features	Medium-high
A-GPS	GPS signal	High

Table 2.1: Accuracy of the positioning methods available in GSM.

Table 2.1 shows a comparison of the accuracy of the positioning methods available in GSM [6, 7, 8]. The two handset-based methods E-OTD and A-GPS provide good results, but they are not adequate for the RESCUECELL system since they require the MT to be able to perform timing measurements or locate itself, which might not be supported by all the MTs. Regarding the network-based methods, Cell-ID and RSSI can be very inaccurate, whereas RF fingerprinting, AOA, TOA and TDOA give the best results. RF fingerprinting methods are not reliable in an emergency situation because the environment could have experienced significant changes and all the previously recorded data would then be useless. On the other hand, AOA techniques do not provide acceptable results in NLOS and multipath propagation conditions. Finally, since TOA methods require synchronization with the MT and knowledge of the transmission time, TDOA is the location technique that suits best our needs since it supports all legacy MTs and gives accurate results.

2.3.1 Parameter measurement for TDOA-based positioning

The basic measurement used in TDOA-based positioning is the time of arrival or propagation delay of the signals sent from the MT. Additionally, the measurement of the RSS can be used to calculate the signal-to-noise ratio (SNR) at the BTS and predict the accuracy of the delay measurement for a given SNR. The GSM protocol already provides the timing advance (TA) and the reception level (RXLEV), two parameters from which the propagation delay and RSS measurements can be obtained.

The propagation delay can be derived from the timing advance (TA), a parameter used to ensure that the bursts transmitted by the MT arrive at the BTS at the correct time [9]. Given the large radius a cell may have and that the slot duration is slightly longer than the burst duration, the MT uses the TA to advance its transmission and compensate the propagation time τ_0. Besides, because the MT synchronizes with the network using the bursts received from the BTS, the propagation time from the BTS to the MT also needs to be taken into account. The value of the TA is the round-trip time, $2\tau_0$, and it is given with a number between 0 and 63 and a resolution of one bit period, which has a duration of 3.692 μs. So, the TA gives the propagation delay with a resolution of $\Delta\tau_0 = \frac{\Delta TA}{2} = 1.85$ μs and the MT-BTS distance in steps of $\Delta R = 550$ m. To obtain the TA values from various BTSs, a handover is forced to each BTS and their TA is measured at different times. With this procedure, the BTSs do not need to be synchronized between them when listening to the transmission from the MT. However, if the BTSs are not synchronized, the MT-BTS synchronization error is not eliminated when the differences between times of arrival are calculated and, therefore, TDOA does not provide any benefit over TOA.

The RXLEV parameter is used in the downlink to indicate the average power of the signal received at the MT from the surrounding BTSs and in the uplink to indicate the power received at the BTS [10]. The measurements from the uplink and the downlink are combined at the BTS and used in downlink power control and handover procedures. The range of the RXLEV measurement goes from -110 dBm to -49 dBm and its value is coded with a number between 0 and 63 and a resolution of 1 dBm.

2.4 Conclusions

Of all available methods in GSM, TDOA-based positioning is the most adequate for the RESCUECELL system since it provides high accuracy and is compatible with all GSM terminals. In the RESCUECELL system, the FAPs serve as the reference points where the TOA and RSS measurements are performed and then forwarded to the CC where the positioning algorithm is run.

Although the GSM protocol provides the TA and RXLEV parameters, even if the FAPs implemented this part of the protocol these parameters would not be accurate enough for our purpose. With a resolution of 1.85 μs in time and 550 m in distance, the TA does not meet the accuracy requirements. On the other hand, since the MT is buried underground, the received signal power is expected to be very low, so the measurement range of the RXLEV parameter may not be sufficient. Moreover, since not all MTs are equipped with the adequate hardware to perform accurate power measurements, it is convenient to perform the measurements at the FAPs.

Since accurate measurements are crucial for a successful localization, custom procedures need to be developed to measure the TOA and the RSS at the FAPs with the required accuracy and reliability in a emergency situation. Therefore, in Chapter 4 we propose several techniques to estimate the TOA and RSS with improved accuracy that will be evaluated using the simulator of the communication link between the MT and the FAP described in Chapter 3.

Chapter 3

Simulator of the communication link between MT and FAP

In this chapter we present the implemented link simulator, which includes a realistic model of the communication link to study the estimation of the TOA and the RSS in a disaster scenario.

3.1 Introduction

In a disaster scenario after an earthquake, the MT is buried underground and communicates with the CC that serves as a BTS. The MT transmits information to the CC in the form of bursts and a FAP listens to the transmitted bursts on the uplink and performs the TOA and RSS measurements. Fig. 3.1 depicts the communication link between the MT, the FAP and the CC.

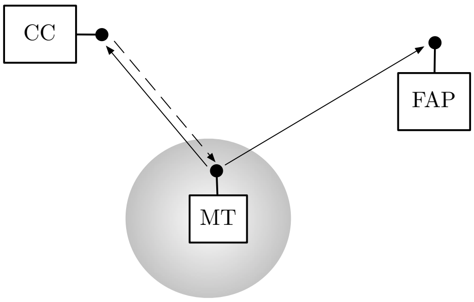

Figure 3.1: Communication link between the MT, the FAP and the CC.

The link simulator models the information transmission from the MT to the FAP through the debris channel. It does not implement the GSM communication protocol as a whole; only the parts involved in the generation, transmission and reception of the GSM signal are considered. Accordingly, the simulator is divided into three main parts: the transmitter of the MT, the debris channel and the receiver of the FAP.

The transmission of a burst from the MT and the detection at the FAP is outlined as follows. First, the transmitter generates the bits of the burst and modulates it with the GMSK modulation. Then, the modulated signal is convolved with the channel, modeling the propagation of the signal. Finally, the signal is filtered and sampled at the receiver. This sampled signal will be used by the estimation algorithms to estimate the TOA and RSS in a later stage. All the operations in the previous steps are performed at baseband frequencies, so all the signals and the channel are represented using their lowpass equivalents.

3.2 Transmitter scheme

Figure 3.2 illustrates the block diagram of a GSM transmitter. Coming from the voice digitizer or other modules, the information bits are first interleaved and encoded in order to prevent transmission errors, then they are incorporated into the burst structure by a multiplexer, and finally they are modulated by the GMSK modulator for baseband transmission. Since the timing information is provided by the raw baseband signal at the receiver and not by the information it contains, there is no need to protect the information against transmission errors. Therefore, we will only model the burst structure and the GMSK modulation.

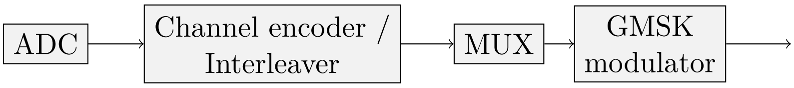

Figure 3.2: Block diagram of a GSM transmitter.

3.2.1 Burst structure

The MT transmits two types of bursts on the uplink: access and normal. The access burst is used to request a frequency channel and a time slot when the MT wants to start or receive a call. This burst is transmitted over the random access channel (RACH), an open channel that any MT in the coverage area can use to access the GSM network. Given that the RACH is a shared channel and the MTs using it are not synchronized with the network yet, access requests from different MTs may collide. Furthermore, since access requests can happen at any time, the BTS does not know exactly when the transmission started. On the other hand, normal bursts are used for information transmission once a connection between the MT and GSM network is established. Hence, the MT only transmits during its assigned slot, which eliminates the risk of collisions with other bursts and gives the BTS a time reference for when the transmission started. Therefore, normal bursts will be used in the link simulator.

The normal burst (Fig. 3.3) is a 148 bit sequence composed of several fields. First, the tail bits at the start and end of the burst allow the MT to ramp up and down its power. Second, the data bits contain the information to be transmitted. Third, the stealing flag indicates whether the data bits are signaling or user data. Last, the training

Tail	Data	S	Training sequence	S	Data	Tail
3	57	1	26	1	57	3

$\longleftrightarrow$

148 bits = 546.12 μs

Figure 3.3: Structure of a normal burst.

sequence is a 26 bit field used at the receiving BTS to estimate the impulse response of the channel and calculate the timing advance. This sequence is always known at the receiver and is carefully chosen so that it provides good channel estimates.

3.2.2 GMSK modulation

Gaussian minimum shift keying (GMSK) is a type of continuous phase modulation derived from the minimum shift keying (MSK) modulation, which is based on another modulation called continuous-phase frequency-shift keying (CPFSK). MSK has desirable qualities such as a constant envelope, a relatively narrow bandwidth and coherent detection capability [11]. However, its power spectrum density does not fall fast enough to avoid co-channel interference. To solve this problem, in GMSK the binary signal to be modulated is passed through a Gaussian shaped filter and then modulated with MSK.

The first step in the modulation process is the conversion of the binary data stream to a non-return to zero (NRZ) representation. In GSM this is done by applying the differential encoding technique and adding an offset to the encoded output [12]. With the input data being $d_i \in \{0,1\}$, the output of the differential encoder is

$$\hat{d}_i = d_i \oplus d_{i-1}, \tag{3.1}$$

where $\oplus$ denotes modulo 2 addition. Then, the data input to the modulator is calculated as

$$a_i = 1 - 2\hat{d}_i \qquad\qquad a_i \in \{-1,1\} \tag{3.2}$$

In a frequency shift keying modulation, the information bits are encoded by varying the instantaneous frequency of the carrier wave. The mathematical expression of a bandpass CPFSK-modulated signal is

$$s(t) = \sqrt{\frac{2E_c}{T_b}} cos(2\pi f_c t + \phi(t)), \tag{3.3}$$

where E_c is the energy per modulating bit, T_b is the bit period, f_c is the carrier frequency and $\phi(t)$ is the information carrying phase of the modulated signal. The CPFSK signal is modulated by the rectangular NRZ bit stream, which shifts the frequency of the signal according to the sign of the bits. The evolution of the phase of the modulated signal is given by the function

$$\phi_{CPFSK}(t) = \pi \frac{h}{T_b} \int_0^t \sum_{i=0}^{\infty} a_i g_{RECT}(\tau - iT_b) d\tau, \tag{3.4}$$

where h is the modulation index, which indicates how much the frequency of the modulated signals differs from the unmodulated carrier frequency, and $g_{RECT}(t)$ is the pulse shaping function defined as

$$g_{RECT}(t) = \begin{cases} 1 & -\frac{T_b}{2} < t < \frac{T_b}{2} \\ 0 & \text{else} \end{cases} \tag{3.5}$$

The expression in (3.4) can be simplified [13] and rewritten as

$$\phi_{CPFSK}(t) = \begin{cases} \phi_o + \pi \frac{h}{T_b} t & a = 1 \\ \phi_o - \pi \frac{h}{T_b} t & a = -1 \end{cases} \tag{3.6}$$

where ϕ_o denotes the accumulated phase change of the previously transmitted symbols. Taking the time derivative of (3.6) and converting to hertz, we obtain the instantaneous frequency shift

$$\Delta f = \frac{h}{2T_b}. \tag{3.7}$$

Thus, a cosine waveform with frequency $f_1 = f_c + \Delta f$ is transmitted when $a_i = 1$ and a frequency $f_2 = f_c - \Delta f$ is used when $a_i = -1$. Also, since this is a continuous phase modulation, the phase of the signal is linearly increased by $\pm\Delta\phi = \pm\pi h$ over the symbol period. In order to facilitate the detection at the receiver, the two used waveforms are required to be orthogonal. This is ensured by setting the frequency shift to a multiple of $\frac{1}{4T_b}$.

MSK is a special case of CPFSK that reduces the bandwidth usage. Since in CPFSK the shaping pulse is rectangular, the power spectrum when a single symbol is transmitted is a sinc-squared function centered at the frequency f_i for $i = \{1, 2\}$. So, the spectrum of a signal representing alternating bit values would be two sinc-squared functions centered at f_1 and f_2. The bandwidth of the signal can be calculated as the separation between f_1 and f_2, plus half the width of the lower sinc, plus half the width of the upper sinc:

$$B_{FSK} = 2\Delta f + \frac{1}{T_b}. \tag{3.8}$$

As the expression shows, a smaller frequency shift results in a lower bandwidth. In MSK, the modulation index h is set to minimize the frequency shift while still maintaining orthogonality. Since Δf has to be a multiple of $\frac{1}{4T_b}$, the value of h that yields the minimum frequency shift is $\frac{1}{2}$. With this modulation index the separation between both frequencies is half the bit rate, so the bandwidth is $B_{MSK} = \frac{3}{2T_b}$, and the phase change when transmitting a symbol is limited to $\pm\frac{\pi}{2}$. Still, the bandwidth reduction achieved is not enough for systems such as GSM. Since rectangular functions are used as shaping pulses, the frequency transitions happen instantly, which produces side lobes that interfere with the adjacent channels.

In GMSK, the NRZ bit stream is filtered with a Gaussian filter to further reduce the bandwidth usage. The Gaussian filter makes the phase shifts smoother, which in turn results in a narrower frequency spectrum and sharper cutoffs. The phase function for a GMSK modulation is

$$\phi_{GMSK}(t) = \pi \frac{h}{T_b} \int_0^t \sum_{i=0}^{\infty} a_i g_{GMSK}(\tau - iT_b) d\tau, \tag{3.9}$$

where $g_{GMSK(t)}$ is the pulse shaping function, defined as the convolution of the rectangular pulse $g_{RECT}(t)$ and a Gaussian function, and the modulation index equals $\frac{1}{2}$. The phase change over a symbol period is $\pm\frac{\pi}{2}$ as in MSK. The transfer function $H(f)$ and the impulse response $h(t)$ of the Gaussian filter are defined as follows

$$H(f) = \exp\left(-\frac{\log_{10}(2)}{2}\left(\frac{f}{W}\right)^2\right) \tag{3.10}$$

$$h(t) = \sqrt{\frac{2\pi}{\log_{10}(2)}} W \exp\left(-\frac{2\pi^2}{\log_{10}(2)} W^2 t^2\right) \tag{3.11}$$

where W is the 3 dB bandwidth of the filter. The response of this Gaussian filter to a rectangular pulse of unit amplitude and duration T, centered at the origin, can be expressed as the difference between two complementary error functions as follows

$$g_{GMSK}(t) = \frac{1}{2}\left[\operatorname{erfc}\left(\pi\sqrt{\frac{2}{\log_{10}(2)}} WT_b \left(\frac{t}{T_b} - \frac{1}{2}\right)\right) - \operatorname{erfc}\left(\pi\sqrt{\frac{2}{\log_{10}(2)}} WT_b \left(\frac{t}{T_b} + \frac{1}{2}\right)\right)\right], \tag{3.12}$$

with the erfc(x) function defined as

$$\operatorname{erfc}(x) = \frac{2}{\sqrt{\pi}} \int_x^{\infty} e^{-t^2} dt. \tag{3.13}$$

The dimensionless time-bandwidth product WT_b in $g_{GMSK}(t)$ is called normalized bandwidth and is a design parameter that determines how fast the side lobes of the power spectrum fall. Figure 3.4 shows the frequency spectrum of the shaping pulse for several values of WT_b. We observe that as the normalized bandwidth decreases, the side lobes become smaller and drop faster while the main lobe becomes narrower. Note that the MSK modulation has an infinite normalized bandwidth since in this case the Gaussian filter would simply be a delta, which has an infinite 3 dB bandwidth. However, these bandwidth improvements come at the expense of introducing intersymbol interference (ISI) in the time domain. As the normalized bandwidth decreases, the Gaussian pulse is spread over a longer time. This causes more than one symbol to be passing through the filter at the same time, consequently interfering between them.

3.2.3 Implementation of the GMSK modulator

There are mainly two ways to implement a GMSK modulator. The first is to filter the bit stream with a Gaussian filter and then apply a frequency modulator with a voltage controlled oscillator (VCO) at a modulation index of $\frac{1}{2}$. This method is fairly simple but

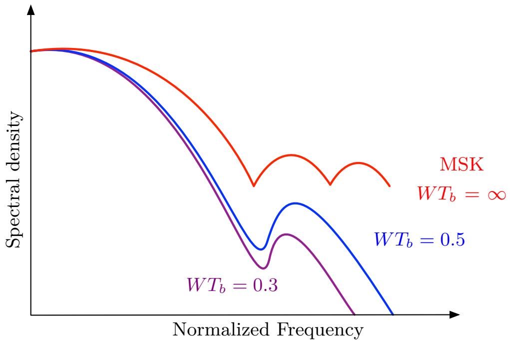

Figure 3.4: Frequency spectrum of the Gaussian shaping pulse for different values of WT_b.

it is not suitable because the tolerances of the VCO drift over time and with temperature, so it is difficult to set an exact modulation index. The second method is to implement it as a quadrature modulator, which allows to maintain the modulation index at exactly $\frac{1}{2}$. The expression of a bandpass signal generated by a quadrature modulator is

$$s(t) = i(t)\cos(2\pi f_c) - q(t)\sin(2\pi f_c), \tag{3.14}$$

where $i(t)$ and $q(t)$ are the in-phase and quadrature components respectively. We can state the bandpass modulated signal in (3.3) as

$$s(t) = \text{Re}\left\{\sqrt{\frac{2E_c}{T_b}} e^{\phi(t)} e^{j2\pi f_c t}\right\} = \text{Re}\left\{u(t) e^{j2\pi f_c t}\right\}, \tag{3.15}$$

where $u(t) = \sqrt{\frac{2E_c}{T_b}} e^{\phi(t)}$ is the equivalent lowpass signal. Applying Euler's formula, $u(t)$ can be expanded into

$$u(t) = \sqrt{\frac{2E_c}{T_b}} \cos(\phi(t)) + j\sqrt{\frac{2E_c}{T_b}} \sin(\phi(t)). \tag{3.16}$$

Substituting (3.16) into (3.15), we obtain

$$s(t) = \sqrt{\frac{2E_c}{T_b}} \cos(\phi(t))\cos(2\pi f_c t) - \sqrt{\frac{2E_c}{T_b}} \sin(\phi(t))\sin(2\pi f_c t). \tag{3.17}$$

Thus, we have the expression of a bandpass quadrature-modulated signal with in-phase component $i(t) = \text{Re}\{u(t)\}$ and quadrature component $q(t) = \text{Im}\{u(t)\}$. Since the link simulator works with baseband transmission, the GMSK modulator will generate the complex baseband equivalent of the GMSK signal, which is given by

$$u(t) = \sqrt{\frac{2E_c}{T_b}} \cos(\phi_{GMSK}(t)) + j\sqrt{\frac{2E_c}{T_b}} \sin(\phi_{GMSK}(t)). \tag{3.18}$$

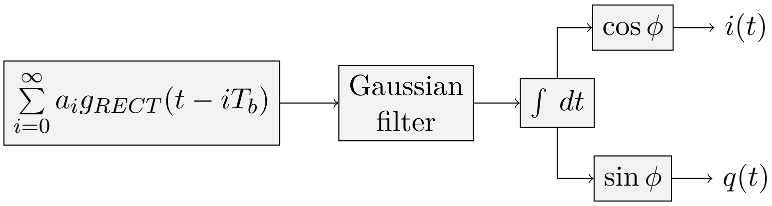

Figure 3.5: Block diagram of the GMSK modulator.

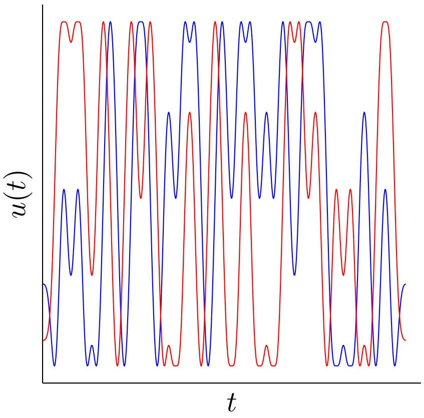

Figure 3.6: Quadrature (blue) and in-phase (red) components of a sample modulated sequence.

The block diagram of the implemented GMSK modulator is shown in Fig. 3.5, and Fig. 3.6 shows a sample modulated sequence with the $i(t)$ component represented in blue and the $q(t)$ component in red.

In GSM, the transmitted information is modulated with GMSK at a bitrate of 270.85 kbps. The chosen normalized bandwidth is 0.3 as a compromise between bandwidth efficiency and ISI. With this value, the 99% of the power of the GMSK-modulated signal lies within a bandpass bandwidth of 250 kHz, and the -3 dB bandwidth is 81.25 kHz. Thus, since the bandwidth of a GSM channel is 200 kHz, co-channel interference is very low. On the time domain, with a normalized bandwidth of 0.3 the Gaussian pulse has a duration of 3 bit periods, hence causing intersymbol interference for the same duration.

The GMSK modulator in the link simulator has been implemented with the GSMsim toolbox [14] for MATLAB. This toolbox provides the necessary functions to implement the elements of a GSM transmitter, depicted in Fig. 3.2, and the elements of the GSM receiver as well. In the simulator, the modulated signal is generated with an amplitude of 1 V and a resolution of 1 ns or, equivalently, 3692 samples per symbol. With this resolution, we are able to adequately model the transmission through the debris channel when the signal is convolved with the impulse response of the channel.

3.3 Debris channel model

In a wireless channel, the radio signals are affected by several phenomenons that degrade the signal quality and the capacity of the communication link. These effects are classified into large scale fading and small scale fading; the large scale fading characterizes the reduction in the received signal power as a function of distance due to path loss or shadowing, while the small scale fading characterizes the rapid variations in the received signal power caused by multipath propagation. Multipath propagation occurs when the transmitted signal reaches the receiver antenna through secondary paths as a result of the scattering, diffraction and reflections caused by objects in the environment such as trees or buildings.

In addition to the characterization of the small and large scale fading effects, the wireless channel can also be classified according to how the signals propagate. Generally, the propagation in a wireless channel can be classified into two modes: line-of-sight (LOS) and non-line-of-sight (NLOS). In a LOS channel, direct visibility exists between the transmitter and the receiver so that the signals travel in a straight line, although multipath propagation may also occur. In contrast, in a NLOS channel the propagation path is partially or totally obstructed by a physical object and the signal can only reach the receiver via multipath propagation. Since in our disaster scenario the MT is buried under a heap of debris, it is affected by both NLOS and multipath propagation.

This section gives an overview of the parameters used in the modeling of the multipath channel and describes the specific characteristics of the debris channel model used in the link simulator.

3.3.1 Mathematical modeling of the multipath channel

Let $s(t) = \mathrm{Re}\{u(t)e^{j2\pi f_c t}\}$ be the transmitted bandpass modulated signal and $r(t)$ the noiseless signal at the receiver after passing through the multipath channel. Since the transmitted signal travels through various paths, the multipath components arrive with different delays and amplitudes. Thus, the received signal is a sum of delayed and weighted copies of the original [15] signal that can be expressed as

$$r(t) = \mathrm{Re}\left\{ \sum_{n=0}^{P(t)} \alpha_n(t) u(t - \tau_n(t)) e^{j(2\pi f_c (t - \tau_n(t)) + \phi_{Dn}(t))} \right\}, \tag{3.19}$$

where $P(t)$ is the number of multipath components, and $\alpha_n(t), \tau_n(t)$ and $\phi_{D_n}(t)$ are the amplitude, delay and Doppler phase shift of the nth path at time t. Besides the attenuation and delay, $u(t)$ suffers a phase change $\phi_n(t) = 2\pi f_c \tau_n(t) - \phi_{Dn}(t)$. If $f_c \tau_n >> 1$, a small change in the path delay can lead to rapid phase variations from path to path. These phase variations cause the received copies to be added constructively or destructively, causing fluctuations of the signal amplitude at the receiver. These variations in amplitude and phase over a short time are known as small scale fading. In comparison, the reduction in received power over longer times and distances due to path loss and shadowing is known as large scale fading.

The received bandpass signal is obtained by convolving the baseband equivalent of the transmitted signal with the baseband equivalent of the channel and multiplying by the carrier frequency. Then, from (3.19) we see that the baseband equivalent of the channel impulse response (CIR) is given by

$$h_c(\tau, t) = \sum_{n=0}^{P(t)} \alpha_n(t) e^{-j\phi_n(t)} \delta(\tau - \tau_n(t)), \tag{3.20}$$

where τ represents the channel response for a given delay and t represents the variation of the channel response with time. The most important parameters for characterizing the wireless channel are the path loss and shadowing, which describe the large scale fading, and the Doppler shift, delay spread and coherence bandwidth, which describe small scale fading effects.

Path loss is the reduction in power of the electromagnetic wave as it propagates through a medium. Path loss models are used to determine the received signal strength at a distance from the transmitter. These models fall into two categories: ray tracing and empirical. Ray tracing models rely on geometry and the dielectric properties of the objects in the environment to calculate the possible propagation paths and their contribution to the received signal power. Thus, using ray tracing models to model heavy multipath propagation can be very difficult. In empirical models, measurements are made in order to characterize the effects of path loss and multipath in a specific environment. Although the small scale fading produced by multipath propagation is included in empirical models, its effects are averaged and the path loss is given as a time independent value. For general analysis, the simplified path loss model offers good results without resorting to complicated calculations. This model gives the path loss as a function of distance as follows:

$$P_L = 10\log_{10}\frac{P_t}{P_r} = K - 10\gamma\log_{10}\frac{d}{d_0}, \tag{3.21}$$

where P_t and P_r are the transmitted and received powers, K is a constant that depends on the antenna and the average channel attenuation, d_0 is a reference distance and γ is the path loss exponent. The values for K, d_0 and γ can be obtained to approximate either an empirical or analytical model.

The other effect that contributes to the large scale fading is the shadowing. Shadowing refers to the random attenuation of the received power caused by the presence of large objects in the propagation path. Since the properties of the blocking objects are generally unknown, statistical models are used to characterize this attenuation. The most commonly used model is the log-normal shadowing model, in which the transmitted to received power ratio $\psi = \frac{P_t}{P_r}$ is a lognormally distributed random variable with mean $\mu_{\psi_{dB}}$ and standard deviation $\sigma_{\psi_{dB}}$. The shadowing can be combined with the path loss in order to characterize the large scale fading with a single model. For instance, if we combine the lognormal shadowing model with the simplified path loss model, the resulting attenuation is

$$10\log_{10}\frac{P_t}{P_r} = K - 10\gamma\log_{10}\frac{d}{d_0} - \psi_{dB}. \tag{3.22}$$

The Doppler shift is the change in frequency of the transmitted signal due to the movement of the transmitter or the receiver. Because of the motion, the propagation environment changes and the channel becomes time variant. Hence, the amplitude α_n and delay τ_n of the multipath components vary with time. The time over which the channel remains invariant is the coherence time, denoted by T_c. The inverse of the coherence time is the Doppler spread D_s, which measures the broadening of the spectrum caused by the Doppler shift.

The delay spread T_m measures the time dispersion caused by multipath propagation. It is defined as the time difference between the arrival of the first component, which may be either LOS or multipath, and the last component. Two metrics that quantify the delay spread are the average and root mean square (RMS) delay spread, denoted by μ_{T_m} and σ_{T_m} respectively, and defined as

$$\mu_{T_m} = \frac{\sum_n \tau_n A_c(\tau_n)}{\sum_n A_c(\tau_n)} \tag{3.23}$$

$$\sigma_{T_m} = \frac{\sum_n (\tau_n - \mu_{T_m}^2) A_c(\tau_n)}{\sum A_c(\tau_n)} \tag{3.24}$$

where $A_c(\tau)$ is the power delay profile (PDP). The PDP is a function that represents the received signal power for a certain time delay and is expressed as

$$A_c(\tau) = \mathbb{E}[h_c^*(\tau, t) h_c(\tau, t)] \tag{3.25}$$

The inverse of the delay spread is the coherence bandwidth B_c, which measures the range of frequencies over which the channel attenuation remains constant.

Depending on the Doppler shift and delay spread, wireless channels can be classified as fast or slow-fading and flat-fading or frequency-selective.

A channel is categorized as a slow fading channel when the coherence time is much larger than the signaling period T_s. Because the channel does not change during T_c, the attenuation and phase change of the transmitted signal remain constant during this period. In contrast, when $T_c << T_s$ the channel is defined as fast fading since the CIR varies rapidly during the transmission of a symbol.

A channel is said to be a flat-fading channel when the delay spread is much smaller than the inverse of the signal bandwidth, i.e. $T_m << B^{-1}$, or when the coherence bandwidth $B_c >> B$. Under these conditions, we can assume that the amplitude of the signal changes very slowly compared to the duration of the CIR and, consequently, $u(t - \tau_n) \approx u(t - \tau)\ \forall\, n$. Thus, (3.19) can be rewritten as

$$r(t) = \mathrm{Re}\left\{ u(t-\tau) e^{j2\pi f_c t} \sum_{n=0}^{P(t)} \alpha_n(t) e^{-j\phi_n(t)} \right\}, \tag{3.26}$$

where the CIR becomes a complex scale factor and the different multipath components are unresolvable. Since $T_m << B^{-1}$, there is very little time spreading and therefore no overlap of a transmitted symbol with the subsequently transmitted symbols. Still, small scale fading occurs because of the destructive interference caused by the multipath components. On the other hand, when $T_m >> B^{-1}$ or $B_c << B$, the channel becomes frequency selective. The time spreading of the symbols produces intersymbol interference and the attenuation of the higher frequencies of the signal power spectrum. Furthermore, the assumption made in (3.26) is no longer valid since the symbol duration is very short compared to the duration of the CIR.

3.3.2 Statistical modeling of the debris channel

The link simulator requires a realistic model of the debris channel in order to reproduce the propagation of the GSM signal in a disaster scenario. In [16, 17, 18], a complete statistical characterization of the debris channel is provided which included statistical models for the large and small scale fading, and the channel impulse response. In the link simulator, only the CIR is needed since the simulator uses the raw signals at the receiver to estimate the TOA and RSS. However, the large and small scale fading models provide us with additional information useful for the configuration of the simulator.

The large scale fading model in [16] takes into account the attenuation caused by the free space propagation and the attenuation caused by the ruins. The Walfisch-Ikegami propagation model, a model suitable for small urban cells, is used to calculate the free space loss as a function of distance and carrier frequency, and it is described as

$$P_L = -35.4 + 26\log_{10}(d) + 20\log_{10}(f_c). \tag{3.27}$$

In the link simulator, the distance between the MT and the FAP is 33 m, which results in a path loss of 63.17 dB. The ruin attenuation was characterized for the case of collapsed buildings and it has an average value of 27.86 dB for the 900 MHz band. So, the total attenuation suffered by the GSM signal is 91 dB. With this attenuation value, the transmitted power and the noise at the receiver we will be able to calculate the expected signal-to-noise ratio at the receiver.

In [17], the statistics for the small scale fading were derived, while a statistical model for the CIR was derived in [18]. These statistics were obtained from measurements of the frequency response of the channel performed in the conditions of a disaster scenario.

The environment in a disaster scenario can be considered quasi-static due to the immobility of the buried people and the slow movement speed of the rescue workers. Thus, the debris wireless channel is time invariant, which also implies that there is no slow fading, and its impulse response becomes

$$h_C(\tau) = \sum_{n=0}^{P} \alpha_n e^{-j\phi_n} \delta(\tau - \tau_n). \tag{3.28}$$

The channel can also be assumed wide sense stationary with uncorrelated scattering components (WSSUS). If we apply the Fourier transform to (3.28), we obtain the channel frequency response (CFR) as

$$H_C(f) = \sum_{n=0}^{P} \alpha_n e^{-j\phi_n} e^{-j2\pi f \tau_n}. \tag{3.29}$$

Using a vector network analyzer (VNA), the CFR of the channel was recorded in [17, 18] in two scenarios that simulated collapsed buildings and stratified rubbles. The two observed frequency bands are the 700 – 1100 MHz band and the 1600 – 2000 MHz band, thus covering the whole frequency range used by GSM900 and GSM1800. In addition, the measurements were also performed in vertical and horizontal polarization modes to simulate the lying and standing position of a cell phone. An omnidirectional antenna was placed under the ruins as a mobile transmitter while the VNA performed the CFR recordings from various locations at distances from 30 to 35 meters. The measured data were then grouped by scenario, frequency band and polarization for the subsequent statistical modeling.

For the characterization of the small scale fading, in [17] the recorded CFRs were converted to the time domain with the inverse discrete Fourier transform (IDFT) in order to obtain the CIR and calculate the parameters $\{\mu_{T_m}, \sigma_{T_m}\}$. The statistical results show that the delay spread is normally below 300 ns and the coherence bandwidth is in the MHz range. Since in GSM the bit period is 3.692 μs and the bandpass channel bandwidth is 200 kHz, the debris channel is not frequency-selective for GSM transmission and is classified as a flat-fading channel.

An autoregressive (AR) model was used in [18] to characterize the amplitude and delay statistics of the multipath components. Although it is possible to do so by using the IDFT, the authors considered that the resulting CIR model order, i.e. the number of multipath components, was too large and a parametric AR method was used instead. When the samples of a signal show linear dependence with the previous samples, an AR model can be used to estimate the peaks of the frequency spectrum of the signal. In [18], the AR modeling technique was applied on the frequency domain instead. The recorded CFRs were modeled as AR processes to estimate the peaks of the temporal response, which correspond to the multipath components.

Different statistical distribution functions were computed from the AR estimated CIRs for every parameter in (3.28) depending on the scenario, with the complete results available in [19]. From the available scenarios, we chose the following for the link simulator: 900 MHz frequency band, horizontal polarization of the transmitting antenna and a ruin scenario composed of stratified ferroconcrete walls.

Table 3.1 shows the statistical distributions of the parameters of the debris channel for the chosen scenario. The parameters provided are the model order P, the excess delay of the first arrival fa_delay, the delay T_n of the rest of multipath components referenced to the first arrival, and the amplitude α_n of the multipath components. The fa_delay parameter measures the excess delay of the first component with respect to LOS propagation, so the delay of the first component is

$$\tau_0 = fa\_delay + \frac{d}{c}, \tag{3.30}$$

where d is the distance between the transmitter and the receiver, and c is the speed of light. The delay of the other components is calculated as $\tau_n = T_n + \tau_0$, and the amplitudes α_n are given by a realization of a random variable whose parameters depend on the value of the delays τ_n.

Parameter	Comment	Distribution
P		Weibull, $\lambda = 15.9752$; $k = 2.2882$
f_{a_delay}	ns	Normal $\mu = 6.0416$; $\sigma = 2.1386$
T_n	ns	Weibull, $\lambda = 48.6810$; $k = 1.2085$
α_n	Time interval (ns)	
	100-115	Lognormal, $\mu = 0.5187$; $\sigma = 1.8192$
	115-130	Lognormal, $\mu = -0.3277$; $\sigma = 0.9000$
	130-145	Lognormal, $\mu = -1.1491$; $\sigma = 0.7601$
	145-160	Lognormal, $\mu = -1.1513$; $\sigma = 0.8357$
	160-175	Lognormal, $\mu = -1.5576$; $\sigma = 0.6569$
	175-190	Lognormal, $\mu = -1.9841$; $\sigma = 0.7553$
	190-205	Lognormal, $\mu = -1.6315$; $\sigma = 0.6962$
	205-250	Normal, $\mu = 0.1047$; $\sigma = 0.0458$

Table 3.1: Statistical distributions of the CIR parameters.

Fig. 3.7 shows an example realization of the CIR of the debris channel generated with the parameters form table 3.1, and Table 3.2 shows the values of the parameters of the multipath components, with the magnitudes multiplied by 10^5. For the generation of this CIR, the distance between the MT and the FAP was set to 33 m, which results in a propagation delay of 100 ns in LOS conditions. Given that the first component of the CIR arrives at 120 ns, we see that there is an additional delay caused by the NLOS propagation.

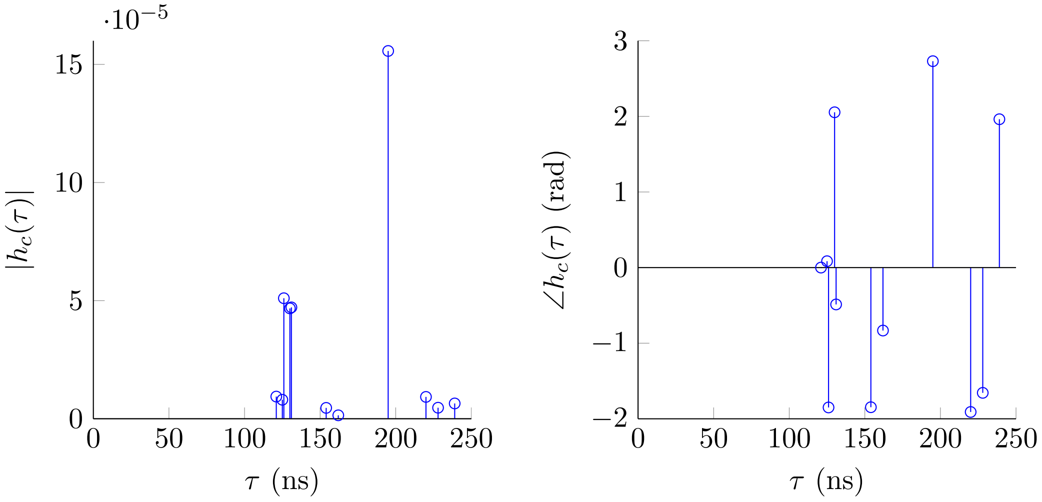

Figure 3.7: Magnitude (left) and phase (right) of a realization of the impulse response of the debris channel.

τ (ns)	α	ϕ (rad)
120.000	0.940	0.000
123.871	2.193	3.042
124.459	0.805	0.084
125.195	0.879	-2.038
125.228	5.102	-1.850
129.252	4.673	2.054
129.913	4.715	-0.487
153.006	0.462	-1.847
160.963	0.147	-0.832
193.816	15.568	2.730
218.551	0.926	-1.909
227.484	0.469	-1.656
238.124	0.649	1.962

Table 3.2: Delay, magnitude and phase of the multipath components of a realization of the debris channel.

3.4 Receiver scheme

A GSM receiver performs the tasks of filtering, sampling, down-converting, demodulating, and decoding the received signal. However, since the simulator operates on the baseband, the signal does not need to be down-converted to a lower frequency. Furthermore the demodulating and decoding steps are not necessary because the estimation algorithms implemented in the link simulator only use the raw signal to perform the estimations. Hence, the GSM receiver in the FAP will consist of a lowpass filter and an analog to digital converter. Since a specific model is required for the noise due to the effect of the lowpass filtering, we will first introduce a standard GSM receiver to explain how the noise model is derived, and then we will describe the receiver implemented in the link simulator and how the noise model is incorporated.

3.4.1 Scheme of a standard GSM receiver

The complex baseband signal at the input of the GSM receiver is the result of the convolution of the transmitted signal with the channel, plus additive Gaussian noise:

$$r(t) = s_r(t) + v(t) = \frac{1}{2}u(t) * h_c(t) + v(t), \tag{3.31}$$

where $s_r(t)$ is the received noiseless signal, $u(t)$ is the transmitted signal, $h_c(t)$ is the baseband CIR and $v(t)$ is the noise.

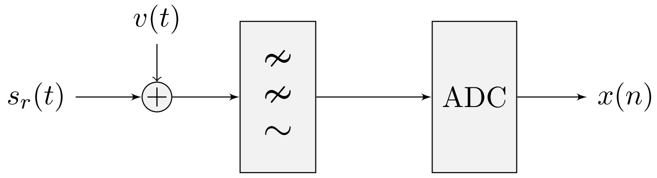

Figure 3.8: Block diagram of the GSM receiver.

The block diagram of the receiver is shown in Fig. 3.8. The received signal is lowpass filtered and then sampled at a sampling frequency f_s. The sampling frequency is defined as $f_s = \frac{\beta}{T_b}$, where β is the oversampling factor, an integer that indicates how many samples per symbol are taken. In the following chapters we will refer to β as the sampling rate, expressed in samples per symbol. The lowpass filter is an ideal filter of bandwidth $B_l = \frac{B_p}{2} = 100$ kHz. Although the bandwidth of the baseband GSM signal can be assumed to be 125 kHz as mentioned in the transmitter model, we can expect the signal not to be largely affected by the filtering since it has a relatively low -3 dB bandwidth of 40.625 kHz and sharp cutoffs. The Gaussian noise is affected by the filtering in that when the sampling frequency exceeds the bandwidth of the filter, the noise at the output of the filter is correlated. Thus, we need to model how the choice of sampling frequency affects the Gaussian noise.

3.4.1.1 Model of the correlated noise at the receiver

Let the noise $\omega(t)$ at the output of the filter be a wide sense stationary random process with distribution $\omega \sim \mathcal{CN}(0, 2N_0B_p)$ and complex baseband equivalent

$$\omega(t) = i_\omega(t) + jq_\omega(t), \tag{3.32}$$

where $i_\omega(t)$ and $q_\omega(t)$ are the in-phase and quadrature components. These are zero-mean wide sense stationary Gaussian baseband random processes with distribution $\omega \sim N(0, N_0B_p)$ and power spectral density N_0 within the range $[-B_p/2, B_p/2]$. Their correlation functions are given by

$$\begin{aligned} R_{i_\omega}(\tau) &= R_{q_\omega}(\tau) = N_0B_p \cdot \mathrm{sinc}(\tau B_p) && (3.33)\\ R_{i_\omega q_\omega}(\tau) &= 0 && (3.34)\end{aligned}$$

as shown in Fig. 3.9, and their variance is

$$\sigma^2_{i_\omega} = \sigma^2_{q_\omega} = N_0B_p. \tag{3.35}$$

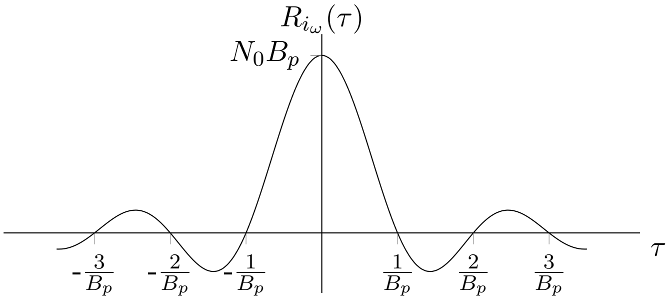

Figure 3.9: Autocorrelation function of $i_\omega(t)$.

Since the $i_\omega(t)$ and $q_\omega(t)$ are Gaussian and uncorrelated between them (3.34), they are independent. When working with a sampled version of $\omega(t)$, i.e. $\omega(n) \equiv \omega(nT_s)$ where $T_s = \frac{T_b}{\beta}$ is the sampling period, the correlation functions of the discrete sequences $i_\omega(n)$ and $q_\omega(n)$ depend on the sampling frequency as follows

$$\begin{aligned} r_{i_\omega}(m) &= \mathbb{E}[i_\omega(n+m) \cdot i^*_\omega(n)] = R_{i_\omega}(mT_s) \equiv r_{q_\omega}(m) && (3.36)\\ r_{i_\omega q_\omega}(m) &= 0 && (3.37)\end{aligned}$$

As observed in Fig. 3.9, if the sampling frequency is $f_s = B_p$, the resulting discrete autocorrelation functions become $r_{i_\omega(n)} = r_{q_\omega(n)} = N_0B_p\delta(n)$ and the noise sequences $i_\omega(n)$ and $q_\omega(n)$ are each uncorrelated zero-mean Gaussian wide sense stationary discrete random processes. If the sampling frequency is $f_s > B_p$, then $i_\omega(n)$ and $q_\omega(n)$ are sequences of correlated noise. Hence, if $f_s = B_p$, the covariance matrix of a noise vector $\boldsymbol{\omega}$ of M samples is $\mathbf{R}_\omega = \mathbb{E}[\boldsymbol{\omega}\boldsymbol{\omega}^H] = 2N_0B_p\mathbf{I}$, where $\mathbf{I}$ is the $M \times M$ identity matrix and the noise vector is defined as

$$\boldsymbol{\omega} = [\omega(0) \cdots \omega(M-1)]^T . \tag{3.38}$$

On the other hand, when $f_s > B_p$ the noise samples are correlated and the noise covariance matrix $\mathbf{R}_\omega$ is no longer diagonal, with entries equal to $\mathbf{R}(l,m) = 2r_{i_\omega}(m-l)$.

With a bit period of 3.692 μs, the minimum frequency at which the GSM signal can be sampled is $f_s = \frac{1}{T_b} = 270.85$ kHz. Since this sampling frequency is greater than the bandpass bandwidth of the lowpass filter, which is 200 kHz, the noise will be correlated. Thus, the covariance matrix of the noise at the output of the GSM receiver is $\mathbf{R}_\omega(l,m) = 2r_{i_\omega}(m-l)$, where the autocorrelation function $r_{i_\omega}(m)$ is defined as

$$r_{i_\omega}(m) = N_0B_p \cdot \mathrm{sinc}(m\frac{T_bB_p}{\beta}). \tag{3.39}$$

3.4.2 Scheme of the implemented GSM receiver

Since the transmitter generates the signal with a resolution of 1 ns, which equals to 3692 samples per symbol, if we were to apply the lowpass filter to the received signal the simulation process would be too time consuming. Therefore, in the implemented receiver the signal is first downsampled to β samples per symbol and then it is filtered and the correlated noise is generated and added directly to the downsampled signal. Fig. 3.10 depicts the block diagram of the implemented receiver. Besides reducing the computational cost with this implementation, by generating the correlated noise and adding it to the downsampled signal we ensure that the noise follows the model previously described. The signal at the output of the receiver to be used by the TOA and RSS estimators is

$$x(n) = s_r(n) * b(n) + \omega(n), \tag{3.40}$$

where $s_r(n)$ is the received signal after the downsampling, $b(n)$ is the discrete-time response of the lowpass filter and $\omega(n)$ is the correlated Gaussian noise.

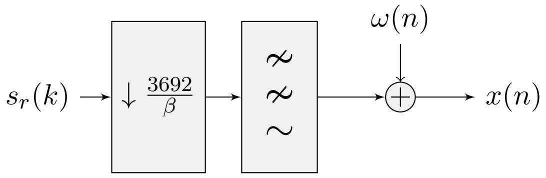

Figure 3.10: Block diagram of the receiver implemented in the link simulator.

3.4.2.1 Implementation aspects of the noise generation at the receiver

In order to obtain the correlated quadrature components, we first generate random vectors $\mathbf{i}'_\omega(n)$ and $\mathbf{q}'_\omega(n)$ with probability density function $N(0, N_oB_p\mathbf{I})$ and pass them through a system that correlates their samples as depicted in Fig. 3.11.

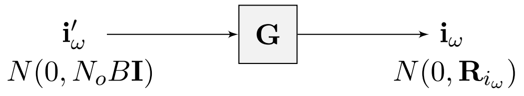

Figure 3.11: Correlated noise generator.

First, we define the desired noise covariance matrix of the form

$$\mathbf{C} = \begin{bmatrix} r_{i_\omega}(0) & r_{i_\omega}(1) & \dots & r_{i_\omega}(N-1) \\ r_{i_\omega}(-1) & r_{i_\omega}(0) & \dots & r_{i_\omega}(N) \\ \vdots & \vdots & \ddots & \vdots \\ r_{i_\omega}(-N+1) & r_{i_\omega}(-N+2) & \dots & r_{i_\omega}(0) \end{bmatrix}$$

where its entries are the values of the autocorrelation function defined in (3.39). Then, we multiply the uncorrelated noise $\mathbf{i}'_\omega$ by a matrix $\mathbf{G}$ so that we obtain the noise vector $\mathbf{i}_\omega = \mathbf{G}\mathbf{i}'_\omega$, with covariance matrix

$$\mathbf{R}_{i_\omega} = \mathbb{E}[\mathbf{i}_\omega \mathbf{i}_\omega^H] = \sigma_{i_\omega}^2 \mathbf{G}\mathbf{I}\mathbf{G}^H. \tag{3.41}$$

Thus, we need to determine the value of $\mathbf{G}$, which can be obtained by diagonalizing the desired autocorrelation matrix as follows

$$\begin{aligned} \sigma_{i_\omega}^2 \mathbf{G}\mathbf{G}^H &= \mathbf{C} \\ \sigma_{i_\omega}^2 \mathbf{G}\mathbf{G}^H &= \mathbf{Q}\mathbf{\Lambda}\mathbf{Q}^H \\ \mathbf{G} &= \frac{1}{\sigma_{i_\omega}} \mathbf{Q}\mathbf{\Lambda}^{\frac{1}{2}} \end{aligned} \tag{3.42}$$

In the implemented receiver, the sampling rate β can take the values $\{1, 2, 4, 13\}$. The value of β modifies the correlation of the noise, so a different matrix $\mathbf{G}$ is generated for each sampling rate.

With regards to the noise power, the GSM standard indicates that the maximum allowed noise power is -62 dBm [20]. Assuming a transmitted power of 30 dBm for a signal of amplitude $A = 1$ V, and an attenuation of 91 dB, as mentioned in the channel model, the signal power at the receiver is -61 dBm. With the signal power and the noise power, we obtain a signal-to-noise ratio (SNR) at the receiver of 2 dB. Given this SNR, in the link simulator we will assume SNR values at the receiver in the [-15,15] range.

Chapter 4

TOA and RSS estimation principles and algorithms

The two parameters to be estimated are the TOA and RSS of a burst sent from the MT and detected at the FAP. In this chapter, we derive the maximum likelihood estimators for the TOA and amplitude and their Cramér-Rao bounds assuming an ideal LOS channel with no multipath. Moreover, in an attempt to improve the estimation accuracy, we also propose a method to estimate the TOA combining bursts from different slots.

4.1 Received signal model for an ideal LOS channel

In the case of an ideal LOS channel, the received signal at the output of the receiver is

$$x(n) = A \cdot p(nT_s - \tau_0) + \omega(n), \tag{4.1}$$

where $p(t)$ is the transmitted pulse, assumed known at the receiver, $A = \alpha_0 e^{j2\pi\tau_0}$ is the amplitude of the CIR and $\omega(n)$ is the filtered and sampled noise with complex normal distribution $\omega \sim \mathcal{CN}(0, 2N_0B_p)$. We assume that the transmitted pulse is a training sequence of length L and constant modulus equal to 1. The signal can also be represented as a vector of length M

$$\mathbf{x} = A\mathbf{p}(\tau_0) + \boldsymbol{\omega}, \tag{4.2}$$

where $\mathbf{p}(\tau_0)$ and $\boldsymbol{\omega}$ are defined as

$$\mathbf{p}(\tau_0) = [0 \ \cdots \ p(-\tau_0) \ \ p(T_s - \tau_0) \ \cdots \ p((L\beta - 1)T_S - \tau_0)]^T \tag{4.3}$$

$$\boldsymbol{\omega} = [\omega(0) \ \cdots \ \omega(M-1)]^T \tag{4.4}$$

and where β is the number of samples per symbol. The time length of the continuous signal $x(t)$ is the length of $p(t)$ plus the delay τ_0 introduced by the LOS channel. After the sampling, the length of the vector $\mathbf{x}$ is $M = \lfloor \frac{\tau_0}{T_s} \rfloor + L\beta$ samples. The noise vector $\boldsymbol{\omega}$ is a complex circular random vector with a complex normal distribution $\boldsymbol{\omega} \sim \mathcal{CN}(0, \mathbf{R}_\omega)$, where $\mathbf{R}_\omega = \mathbb{E}[\boldsymbol{\omega}^H\boldsymbol{\omega}]$ is the $M \times M$ noise covariance matrix. .

The likelihood function of $\boldsymbol{\theta} = \{A, \tau_0\}$ given $\mathbf{x}$, which will be used in the derivation of the CRB and the ML estimators, is

$$f_{\mathbf{x}}(\mathbf{x}|\boldsymbol{\theta}) = \frac{1}{\pi^M |\mathbf{R}_w|} e^{-(\mathbf{x}-A\mathbf{p}(\tau_0))^H \mathbf{R}_w^{-1} (\mathbf{x}-A\mathbf{p}(\tau_0))}, \tag{4.5}$$

where $\{A, \tau_0\}$ are the unknown parameters to be estimated.

4.2 Cramér-Rao bound for amplitude and TOA estimation

The CRB is the lowest variance an unbiased estimator may achieve and, therefore, it is used as a benchmark for the estimators. Additionally, when a closed expression is obtained, it may give insight into the parameters that impact on the performance of the estimators. In this section we examine the CRB expressions for the TOA and amplitude, i.e, $\boldsymbol{\theta} = \{A, \tau_0\}$, assuming the received signal in (4.1) and the likelihood function in (4.5).

The expressions of the CRBs for the unknown parameters A and τ_0, derived in Appendix A, are

$$\sigma_{\hat{A}}^2 \geq \frac{1}{\mathbf{p}^H(\tau_0)\mathbf{R}_w^{-1}\mathbf{p}(\tau_0) - \frac{1}{2} \frac{|\mathbf{p}^H(\tau_0)\mathbf{R}_w^{-1} \frac{\partial \mathbf{p}(\tau_0)}{\partial \tau_0}|^2}{\frac{\partial \mathbf{p}^H(\tau_0)}{\partial \tau_0} R_w^{-1} \frac{\partial \mathbf{p}(\tau_0)}{\partial \tau_0}}} \tag{4.6}$$

$$\sigma_{\hat{\tau}_0}^2 \geq \frac{1}{2|A|^2 \frac{\partial \mathbf{p}^H(\tau_0)}{\partial \tau_0} \mathbf{R}_w^{-1} \frac{\partial \mathbf{p}(\tau_0)}{\partial \tau_0} - \frac{|A|^2 \; |\mathbf{p}^H(\tau_0)\mathbf{R}_w^{-1} \frac{\partial \mathbf{p}(\tau_0)}{\partial \tau_0}|^2}{\mathbf{p}^H(\tau_0)\mathbf{R}_w^{-1}\mathbf{p}(\tau_0)}} \tag{4.7}$$

It is important to remark that the bounds in (4.6) and (4.7) are only valid when the sampling frequency f_s is equal to the bandpass filter bandwidth $B_p = 200$ kHz. When the signal is sampled at a higher rate, the noise is not only correlated but the rows of $\mathbf{R}_\omega$ become linear dependent, thus making $\mathbf{R}_\omega$ non-invertible. Therefore, the CRB cannot be calculated when $f_s > B_p$. In our GSM link, the sampling rate β is an integer with a minimum value of 1, so the minimum sampling frequency is $f_s = \frac{1}{T_b} = 270.85$ kHz and, therefore, the noise is always correlated. Still, we will calculate the CRBs assuming uncorrelated noise with covariance matrix $\mathbf{R}_\omega = 2N_0B_p\mathbf{I}$ for any sampling rate β and use them as benchmarks in the simulations. Substituting $\mathbf{R}_\omega$ in (4.6) and (4.7) and knowing that the SNR of the received signal is $SNR = \frac{|A|^2}{2N_0B_p}$ and the energy of the transmitted pulse is $E_p = ||\mathbf{p}(\tau_0)||^2$, we can rewrite (4.6) and (4.7) as

$$\sigma_{\hat{A}}^2 \geq \frac{1}{\frac{E_p}{2N_0B_p} - \frac{1}{4N_0B_p} \frac{\left|\mathbf{p}^H(\tau_0)\frac{\partial \mathbf{p}(\tau_0)}{\partial \tau_0}\right|^2}{\left|\left|\frac{\partial \mathbf{p}(\tau_0)}{\partial \tau_0}\right|\right|^2}} \tag{4.8}$$

$$\sigma^2_{\hat{\tau}_0} \geq \frac{1}{2SNR \left\|\frac{\partial \mathbf{p}(\tau_0)}{\partial \tau_0}\right\|^2 - SNR \frac{\left|\mathbf{p}^H(\tau_0)\frac{\partial \mathbf{p}(\tau_0)}{\partial \tau_0}\right|^2}{E_p}} \tag{4.9}$$

In the numerical results, we observed that the second term in the denominators of (4.8) and (4.9) is much smaller than the first one. Hence, we can discard the second term in the denominators in order to give some insight into the expressions, which results in:

$$\sigma^2_{\hat{A}} \gtrapprox \frac{2N_0B_p}{E_p} \tag{4.10}$$

$$\sigma^2_{\hat{\tau}_0} \gtrapprox \frac{1}{2SNR \left\|\frac{\partial \mathbf{p}(\tau_0)}{\partial \tau_0}\right\|^2} \tag{4.11}$$

With the simplified expressions, we are able to identify which parameters have an impact on the CRBs. Given that in our case the transmitted pulse has a constant modulus equal to one, the energy of the sampled pulse at the receiver is $E_p = \sum_{i=0}^{M-1} |p_i|^2 = L\beta$. Therefore, an increase in the length of the training sequence yields a lower CRB for the amplitude estimation. In the same way, a higher L also lowers the CRB for $\hat{\tau}_0$. If we define the discrete delay $n_0 = \lfloor \frac{\tau_0}{T_s} \rfloor$ and expand the norm in the denominator of (4.11), we obtain

$$\begin{aligned}
\left\|\frac{\partial \mathbf{p}(\tau_0)}{\partial \tau_0}\right\|^2 &= \sum_{n=n_0}^{M-1} \left|\frac{\partial p(nT_s-\tau_0)}{\partial \tau_0}\right|^2 = \sum_{n=n_0}^{M-1} \left|\frac{\partial p(t)}{\partial t}\right|^2 \Bigg|_{t=nT_s-\tau_0} \\
&= \sum_{n=0}^{L\beta-1} \left|\frac{\partial p(t)}{\partial t}\right|^2 \Bigg|_{t=nT_s} = \frac{1}{T_s}\int_0^{LT_b} \left|\frac{\partial p(t)}{\partial t}\right|^2 \\
&= \frac{\beta}{T_b}\int_0^{LT_b} \left|\frac{\partial p(t)}{\partial t}\right|^2 .
\end{aligned} \tag{4.12}$$

Although the modulus of $p(t)$ is constant, its quadrature components are not and in the GMSK modulation their value always varies from symbol to symbol. Hence, the derivative in (4.12) is nonzero for $t > \tau_0$ and the addition of more symbols to the training sequence increases the value of the norm. On the other hand, with a higher sampling rate the number of samples becomes larger and the energy of the sampled pulse increases. Therefore, the CRBs for both estimators are lowered. A rapidly varying signal would also yield a lower CRB in the case of the TOA estimation, although this would require a higher signal bandwidth. Moreover, we observe in both (4.10) and (4.11) that a reduction in the noise power decreases the CRB, and that for the TOA estimation an increase in transmitted power also lowers the CRB.

With the CRBs as benchmarks we are able to set a goal for the variance of the amplitude and TOA estimators. The expressions of the CRBs tell us that the variance might be improved by increasing the training sequence length, the SNR and the signal bandwidth. Of the three parameters, only the sequence length and the SNR can be modified in a custom implementation of the GSM link. Furthermore, there exists the possibility that, despite the correlated noise, a higher sampling rate would also reduce the variance. Hence, we will evaluate the performance of the estimators for several combinations of β, L and SNR and determine how the values of these parameters impact on the estimation accuracy.

4.3 Maximum likelihood TOA and amplitude estimation

The ML estimation is a method to estimate the parameters of a statistical model. A ML estimator is unbiased and, given a sample size that tends to infinity, its variance converges to the CRB.

Given the received signal $\mathbf{x}$ defined in (4.1), the ML estimates for $\boldsymbol{\theta} = \{A, \tau_0\}$ can be obtained by maximizing the likelihood function of $\mathbf{x}$:

$$\hat{\boldsymbol{\theta}}^{ML} = \arg\max_{\boldsymbol{\theta}} \ \ln f_x(\mathbf{x}|\boldsymbol{\theta}) \quad = \arg\min_{A,\tau_0} \ \ln\pi|\mathbf{R}_w| + (\mathbf{x} - A\mathbf{p}(\tau_0))^H \mathbf{R}_w^{-1}(\mathbf{x} - A\mathbf{p}(\tau_0)). \tag{4.13}$$

In order to get $\hat{\tau}_o^{ML}$, we will first calculate the estimator $\hat{A}^{ML}$, which can be derived by maximizing with respect to A as follows

$$\begin{aligned}
\frac{\partial}{\partial A^*}\ln f_x(\mathbf{x}|\boldsymbol{\theta}) &= 0 \\
\frac{\partial}{\partial A^*}(\mathbf{x} - A\mathbf{p}(\tau_0))^H \mathbf{R}_w^{-1}(\mathbf{x} - A\mathbf{p}(\tau_0)) &= 0 \\
\mathbf{p}^H(\tau_0)\mathbf{R}_w^{-1}(\mathbf{x} - A\mathbf{p}(\tau_0)) &= 0 \\
\hat{A}^{ML} &= \frac{\mathbf{p}^H(\tau_0)\mathbf{R}_w^{-1}\mathbf{x}}{\mathbf{p}^H(\tau_0)\mathbf{R}_w^{-1}\mathbf{p}(\tau_0)}
\end{aligned} \tag{4.14}$$

With this estimator, the RSS can easily be calculated as $RSS = |\hat{A}^{ML}|^2$. Now, if we substitute $\hat{A}^{ML}$ into (4.13) and maximize with respect to τ_0, we have:

$$\begin{aligned}
\hat{\tau}_o^{ML} &= \arg\max_{\tau_0} \ -\ln\pi|\mathbf{R}_w| - (\mathbf{x} - A\mathbf{p}(\tau_0))^H \mathbf{R}_w^{-1}(\mathbf{x} - A\mathbf{p}(\tau_0)) \\
&= \arg\max_{\tau_0} \ A\mathbf{x}^H\mathbf{R}_w^{-1}\mathbf{p}(\tau_0) + A^*\mathbf{p}^H(\tau_0)\mathbf{R}_w^{-1}\mathbf{x} - |A|^2\mathbf{p}^H(\tau_0)\mathbf{R}_w^{-1}\mathbf{p}(\tau_0) \\
&= \arg\max_{\tau_0} \ 2\frac{|\mathbf{x}^H\mathbf{R}_w^{-1}\mathbf{p}(\tau_0)|^2}{\mathbf{p}^H(\tau_0)\mathbf{R}_w^{-1}\mathbf{p}(\tau_0)} - \frac{|\mathbf{x}^H\mathbf{R}_w^{-1}\mathbf{p}(\tau_0)|^2}{|\mathbf{p}^H(\tau_0)\mathbf{R}_w^{-1}\mathbf{p}(\tau_0)|^2}\mathbf{p}^H(\tau_0)\mathbf{R}_w^{-1}\mathbf{p}(\tau_0) \\
&= \arg\max_{\tau_0} \ |\mathbf{x}^H\mathbf{R}_w^{-1}\mathbf{p}(\tau_0)|^2
\end{aligned} \tag{4.15}$$

Assuming that the noise is uncorrelated and its covariance matrix is $\mathbf{R}_\omega = 2N_0B_p\mathbf{I}$, the estimators (4.14) and (4.15) become

$$\hat{A}^{ML} = \frac{\mathbf{p}^H(\tau_0)\mathbf{x}}{E_b} \tag{4.16}$$

$$\hat{\tau}_o^{ML} = \arg\max_{\tau} \ |\mathbf{x}^H \mathbf{p}(\tau)|^2 \tag{4.17}$$

where τ is the delay parameter of the TOA estimator. The ML estimator of A returns the estimated amplitude for the delay τ_0, while the ML estimator of τ_0 performs a search of the delay τ that applied to the vector $\mathbf{p}$ maximizes the product $\mathbf{x}^H \mathbf{p}(\tau)$. In theory, this product reaches its maximum value when $\tau = \tau_0$ so that $\mathbf{x}^H \mathbf{p}(\tau_0) = A \, ||\mathbf{p}||^2 + \boldsymbol{\omega}^H \mathbf{p}(\tau_0)$. However, due to the noise, the maximum will not always be located at $\tau = \tau_0$.

Although in our system the noise is always correlated, we will use the TOA and amplitude estimators derived assuming uncorrelated noise and investigate in the simulations how the noise correlation affects the estimations.

4.3.1 Implementation of the TOA and amplitude estimators

In a practical implementation of the ML estimators, $\mathbf{p}(\tau)$ is a copy of the transmitted training sequence sampled at β samples per symbol and delayed by τ . Since $\mathbf{p}$ is discrete, it is only possible to apply a delay of an integer number of samples. Hence, the TOA estimator in (4.17) becomes a search for an integer delay

$$\hat{k}_0 = \arg\max_{k} \ |\mathbf{x}^H \mathbf{p}(k)|^2, \tag{4.18}$$

where $\mathbf{p}$ is redefined as

$$\mathbf{p}(k) = \left[0 \ \cdots \ p(-k) \ \ p(1-k) \ \cdots \ p(L\beta - 1 - k)\right]^T. \tag{4.19}$$

This estimator can be implemented as a correlator that looks for the position of the maximum of the cross-correlation between the received signal and the sampled copy $\mathbf{p}(k)$. Fig. 4.1 shows the block diagram of the TOA estimator implemented in the link simulator, which is composed of a correlator, a peak detector and an interpolator. The estimation of the delay k_0 at the output of the peak detector is

$$\hat{k}_0 = \arg\max_{k} \ |r_{xp}(k)|^2 = \arg\max_{k} \ \left| \sum_{n=0}^{M} x^*(n) p(n-k) \right|^2. \tag{4.20}$$

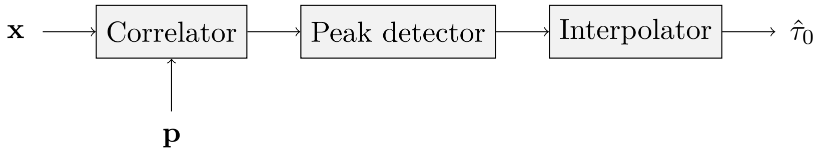

Figure 4.1: Block diagram of the TOA estimator at the receiver.

Once $\hat{k}_0$ is obtained, $\hat{\tau}_0$ can be calculated as $\hat{\tau}_0 = \hat{k}_0 T_s$. Since $\hat{\tau}_0$ can only be a multiple of T_s, there is a loss in resolution of the TOA estimator that can introduce a large bias in the estimation result, as it will be shown later in the simulations. To solve this problem, an interpolator is used at the output of the peak detector. An approximation of the real peak of the correlation function is obtained after interpolating three values at the output of the correlator: the maximum and both its preceding and following values, applying the following interpolator

$$f(x) = a + bx + cx^2 \tag{4.21}$$

where a, b, and c are parameters fitting the measured correlation [21]. These parameters are obtained by solving the following system of equations

$$\begin{bmatrix} 1 & \hat{k}_0 - 1 & (\hat{k}_0 - 1)^2 \\ 1 & \hat{k}_0 & \hat{k}_0^2 \\ 1 & \hat{k}_0 + 1 & (\hat{k}_0 + 1)^2 \end{bmatrix} \begin{bmatrix} a \\ b \\ c \end{bmatrix} = \begin{bmatrix} r_{xp}(\hat{k}_0 - 1) \\ r_{xp}(\hat{k}_0) \\ r_{xp}(\hat{k}_0 + 1) \end{bmatrix}$$

The estimate of the time delay can be found by detecting the vertex of the parabola

$$\hat{\tau}_0 = -b/2a. \tag{4.22}$$

A graphical example of the effect of the interpolator is shown in Fig. 4.2. The dashed line represents the output of the correlator, and the solid line shows the parabolic interpolation using the maximum and its two adjacent values.

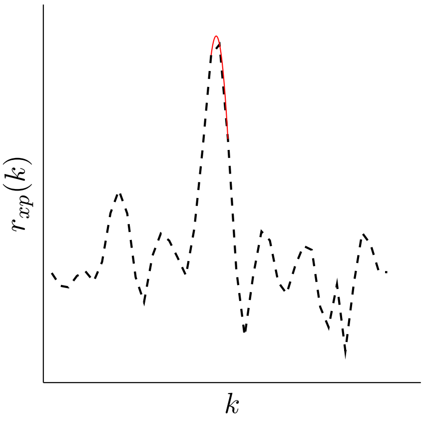

Figure 4.2: Interpolation of the correlation maximum.

In the ML amplitude estimator from (4.16) the received signal is multiplied by a copy of the transmitted training sequence and then divided by E_b. Given that the copy of the training sequence is delayed by τ_0, the resulting estimation is

$$\hat{A}^{ML} = \frac{A \cdot E_b + \mathbf{p}^H(\tau_0)\boldsymbol{\omega}}{E_b} = A + \frac{\mathbf{p}^H(\tau_0)\boldsymbol{\omega}}{E_b}. \tag{4.23}$$

However, in a real implementation of the amplitude estimator the delay τ_0 is unknown, so the delay of the copy of the training sequence must be specified as a parameter. Fig. 4.3

shows the block diagram of the amplitude simulator implemented the link simulator. The delay of the received burst is first estimated using the TOA estimator and then it is passed to the amplitude estimator. Again, since it is only possible to apply integer delays, the delay $\hat{k}_0$ estimated before the interpolation is used.

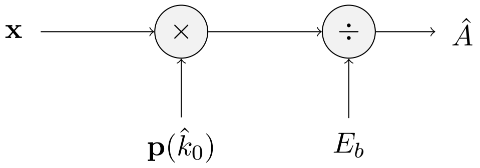

Figure 4.3: Block diagram of the amplitude estimator at the receiver.

The delay and amplitude estimation processes can be resumed as follows. The sampled signal $x(n)$ is correlated with the discrete version of the known pulse, $p(n)$. The instant k_0 where the absolute value of the cross correlation is maximum is determined. This maximum and its adjacent values are used to interpolate the cross correlation using (4.21), and recalculate the maximum again. The value at the output of the interpolator corresponds to the estimate of the time delay $\hat{\tau}_0$, according to (4.22). Finally the estimate $\hat{k}_0$ is substituted in the expression in (4.16) to obtain an estimation of the amplitude of the received signal.

Given that in GSM the MT transmits the bursts in individual and independent time slots, the accuracy of the estimation can be improved by combining the bursts form several slots. An estimation technique that combines the bursts from two slots and performs a joint TOA estimation is proposed in section 4.4.

4.4 ML TOA estimation combining two slots

One way of improving the performance of a communications system is the use of time diversity. This technique consists in transmitting the same signal at various time instants so that these replicas may be combined at the receiver to improve the signal quality. Although in general time diversity helps mitigate the effect of temporary fading or interferences, this not the case for our disaster scenario because the time coherence of the channel is much larger than the signaling time.

Since in GSM communications the MT transmits bursts at different time slots, it is possible to increase time diversity by means of combining several slots. As the amount of data is increased, this may result in a reduced variance of the delay estimation. In this section we consider the case of combining the bursts from $N = 2$ independent time slots. Again, we resort to the ML estimator of the time delay derived under the assumption of an ideal channel.

Let the signals from two different slots sensed and sampled at a given FAP be given by

$$\mathbf{x}_1 = A_1\mathbf{p}(\tau_0) + \boldsymbol{\omega}_1 \tag{4.24}$$
$$\mathbf{x}_2 = A_2\mathbf{p}(\tau_0 + \Delta) + \boldsymbol{\omega}_2 \tag{4.25}$$

The two signals $\mathbf{x}_1$ and $\mathbf{x}_2$ are replicas of a known pulse, delayed by τ_0 and $\tau_0 + \Delta$ respectively, plus zero-mean additive Gaussian noise. The term Δ in $\mathbf{x}_2$ is related to the synchronization error between the MT and the BTS, which, according to the standard can be up to ±1 bit periods [9]. This means that the burst emitted by the MT can arrive up to 3.692 μs before or after its assigned time slot starts. Taking the signal from the first slot as a reference, Δ indicates the time shift of the second signal with respect to the first one. As a consequence, the two slots transmitted by the MT cannot be directly combined due to this unknown relative time shift. Therefore, the delays τ_0 and Δ should be jointly estimated.

In the approach proposed here, a joint maximum likelihood estimation of the propagation delay on the received signals is performed. Let $\boldsymbol{\theta} = \{\tau_0, \Delta, A_1, A_2\}$ denote the set of unknown parameters. Provided that the signals are statistically independent, their joint likelihood function is

$$f(\mathbf{x}_1, \mathbf{x}_2|\boldsymbol{\theta}) = f(\mathbf{x}_1|\boldsymbol{\theta}_1) f(\mathbf{x}_2|\boldsymbol{\theta}_2) \tag{4.26}$$
$$= K \cdot \exp\Big[-(\mathbf{x}_1 - A_1\mathbf{p}(\tau_0))^H \mathbf{R}_{\omega_1}^{-1}(\mathbf{x}_1 - A_1\mathbf{p}(\tau_0)) \tag{4.27}$$
$$- (\mathbf{x}_2 - A_2\mathbf{p}(\tau_0+\Delta))^H \mathbf{R}_{\omega_2}^{-1}(\mathbf{x}_2 - A_2\mathbf{p}(\tau_0+\Delta))\Big] \tag{4.28}$$

where $K = (\pi^{2N}|\mathbf{R}_{\omega_1}||\mathbf{R}_{\omega_2}|)^{-1}$. For simplicity, we will assume that $\boldsymbol{\omega}_1$ and $\boldsymbol{\omega}_2$ are AWGN with variances $\sigma_{\omega_1}^2$ and $\sigma_{\omega_2}^2$ respectively. Then, the log-likelihood function to be maximized is given by

$$\ln f(\mathbf{x}_1, \mathbf{x}_2|\boldsymbol{\theta}) = \ln K - \frac{|\mathbf{x}_1 - A_1\mathbf{p}(\boldsymbol{\tau_0})|^2}{\sigma_{\omega_1}^2} - \frac{|\mathbf{x}_2 - A_2\mathbf{p}(\boldsymbol{\tau_0} + \boldsymbol{\Delta})|^2}{\sigma_{\omega_2}^2} \tag{4.29}$$

Deriving (4.29) with respect to A_1^* and A_2^* and equating to zero we obtain the ML estimate for each amplitude, i.e.,

$$\hat{A}_1^{ML} = \frac{\mathbf{p}^H(\tau_0)\mathbf{x}_1}{E_p} \tag{4.30}$$

$$\hat{A}_2^{ML} = \frac{\mathbf{p}^H(\tau_0 + \Delta)\mathbf{x}_2}{E_p} \tag{4.31}$$

Substituting $\hat{A}_1^{ML}$ and $\hat{A}_2^{ML}$ in (4.29) yields

$$\begin{aligned}\ln f(\mathbf{x}_1, \mathbf{x}_2|\tau_0, \Delta) &= \ln K - \frac{1}{\sigma_{\omega_1}^2}\left|\mathbf{x}_1 - \frac{\mathbf{p}^H(\tau_0)\mathbf{x}_1\mathbf{p}(\tau_0)}{E_p}\right|^2 - \frac{1}{\sigma_{\omega_2}^2}\left|\mathbf{x}_2 - \frac{\mathbf{p}^H(\tau_0+\Delta)\mathbf{x}_2\mathbf{p}(\tau_0+\Delta)}{E_p}\right|^2 \\ &= \ln K - \frac{1}{\sigma_{\omega_1}^2 E_p^2}\left|E_p\mathbf{x}_1 - \mathbf{p}^H(\tau_0)\mathbf{x}_{1|}\mathbf{p}(\tau_0)\right|^2 - \frac{1}{\sigma_{\omega_2}^2 E_p^2}\left|E_p\mathbf{x}_2 - \mathbf{p}^H(\tau_0+\Delta)\mathbf{x}_2\mathbf{p}(\tau_0+\Delta)\right|^2 \\ &= \ln K + \frac{1}{\sigma_{\omega_1}^2 E_p}\left(E_p||\mathbf{x}_1||^2 - \left|\mathbf{p}^H(\tau_0)\mathbf{x}_1\right|^2\right) + \frac{1}{\sigma_{\omega_2}^2 E_p}\left(E_p||\mathbf{x}_2||^2 - \left|\mathbf{p}^H(\tau_0+\Delta)\mathbf{x}_2\right|^2\right)\end{aligned} \tag{4.32}$$

Since the signals are received at the same FAP, it is reasonable to assume that the noise power does not differ from one slot to the other. Furthermore, the terms containing $\sigma_{\omega_1}^2$, $\sigma_{\omega_2}^2$, E_p and $|\mathbf{x}_i|$ in (4.32) are considered nuisance parameters for the maximization of $\ln f(\mathbf{x}_1, \mathbf{x}_2|\tau, \Delta)$ so that the ML estimates for τ and Δ are obtained as follows

$$\{\hat{\tau}_0, \hat{\Delta}\}^{ML} = \arg\max_{\tau,\delta}\left|\mathbf{p}^H(\tau)\mathbf{x}_1\right|^2 + \left|\mathbf{p}^H(\tau+\delta)\mathbf{x}_2\right|^2, \tag{4.33}$$

where τ and δ are the parameters of the estimator for the propagation delay and the relative delay respectively. Note that (4.33) is the summation of the cross correlation of the received slots $\mathbf{x}_1$ and $\mathbf{x}_2$ with the reference pulse shifted τ and $\tau + \delta$, respectively. The resulting estimator is therefore a two-dimensional search of the maximum of (4.33) for all values of τ and δ. As for the time delay estimation with one single slot, the fact that we deal with a sampled signal would introduce a severe bias in the estimation of τ_0. Therefore, we propose to use a two dimensional interpolation function that compensates for this problem. The interpolation method consists in a parabolic interpolation applied to both dimensions of the ML estimation function. First, the values of δ that maximize the ML function for each τ are interpolated and then substituted into the ML function. Next, another interpolation is performed around the maximum, resulting in the delay estimate $\hat{\tau}_0$.

4.5 Conclusions of the TOA and amplitude estimation

In this chapter we have derived the ML estimators for the TOA and the amplitude and have described their implementation in the link simulator. The TOA estimator is implemented as a correlator that calculates the cross correlation between the received signal and a copy of the training sequence and finds the peak of the cross correlation function. Additionally, an interpolator is added to improve the resolution of the estimator. A ML TOA estimator that combines the signals from two slots to reduce the estimation variance has also been proposed. On the other hand, the amplitude estimator takes the result of the TOA estimation as an input parameter and calculates the amplitude of the received signal. Although the estimators were derived assuming an ideal LOS channel and uncorrelated noise, in the simulations their performance will be also evaluated in the realistic conditions of the communication link, that is, with the debris channel and correlated noise.

We have also derived the Cramér-Rao bounds for the TOA and amplitude estimators, which will be used as benchmarks for the estimation variance in the simulations. Moreover, the expressions of the CRBs show that an increase in the sampling rate, training sequence length and SNR might improve the variance, thus their effect will be studied in the simulations.

Chapter 5

Simulation results of the TOA and amplitude estimation

In this chapter we present the results of the simulations performed in different configurations with the link simulator introduced in Chapter 3 and the estimation techniques derived in Chapter 4. With the link simulator, we are able to realistically reproduce the conditions of the RESCUECELL scenario to analyze the factors that impact on the performance of the TOA and amplitude estimators, and foresee some of the challenges we might encounter in a real implementation.

5.1 Simulator setup

The implemented link simulator reproduces the transmission of a burst from the MT to the FAP and the posterior estimation of the TOA and the amplitude. To evaluate the performance of the estimators, the transmission and estimation process is repeated over a number of realizations and the performance metrics are calculated from the estimation results. These metrics are the bias and the variance, given by

$$\text{bias}(\hat{\theta}) = \left|\mathbb{E}[\hat{\theta} - \theta]\right|, \qquad \text{var}(\hat{\theta}) = 10\log_{10}(\mathbb{E}[|\hat{\theta} - \mathbb{E}[\hat{\theta}]|^2])$$

The bias gives the average estimation error and the variance indicates how spread out the estimated values are.

The link simulator allows for different configuration options that can be combined to simulate a specific scenario. First, the TOA estimation can be performed with the received signals from one or two slots, whereas the amplitude estimation is performed with a single slot. Second, two types of bursts can be transmitted: a burst consisting of a random training sequence or a complete normal burst. The random training sequences are random bit sequences of length L, while the normal burst follows the format defined in section 3.2.1. When only the training sequence is transmitted, a single random training sequence is generated and used in all the realizations. With the normal burst, the 26 bits of the training sequence are predefined and do not change, while the rest of the bits in the burst are randomized in each realization. Last, the channel can be an ideal LOS channel with no multipath or a realization of the debris channel. Since we want to evaluate the performance of the TOA and amplitude estimators, the channel impulse response is the same in all the realizations and only a new vector of correlated Gaussian noise is generated every time.

In the different scenarios, the performance metrics are presented as a function of several parameters, which are the SNR, the sampling rate β expressed as the number of samples per symbol and the length of the training sequence L.

5.2 Simulation results of the ML TOA estimator

The performance of the TOA estimator is evaluated in different scenarios. Initially, we consider the conditions for which the estimator was derived, that is, a single slot, an ideal LOS channel, and a transmitted burst consisting of only the training sequence. In these conditions we evaluate whether the ML estimator is adequate given the specifications of our system and also assess the impact of the various parameters and the correlated noise. Next, a second slot is added to the initial configuration to determine whether the estimation results improve when two slots are combined. Once the ML estimator is validated and deemed adequate for our purposes, we study its performance in realistic conditions with the debris channel. In this setting, we first consider the transmission of a random training sequence to see how the NLOS and multipath propagation affect the estimation performance. Finally, we also evaluate the performance in the case that a complete normal burst is transmitted and used for TOA estimation.

The performance metrics computed for the simulations are the bias and the variance, given respectively by

$$\text{bias}(\hat{\tau}_0) = |\mathbb{E}[\hat{\tau}_0 - \tau_0]| \,, \qquad \text{var}(\hat{\tau}_0) = 10\log_{10}(\mathbb{E}[|\hat{\tau}_0 - \mathbb{E}[\hat{\tau}_0]|^2])$$

where τ_0 is the propagation delay of the first arrival and $\hat{\tau}_0$ is the delay estimated by the ML TOA estimator. The results are averaged over 10000 independent realizations in each of the simulated scenarios.

5.2.1 Simulation results in ideal LOS conditions with a single slot

In this first scenario we validate our implementation of the ML TOA estimator as a correlator plus an interpolator and examine how the choice of sampling rate and training sequence length impact the bias and variance. For the simulations of a pure delay in LOS conditions, the following sets of parameter values are chosen

- $\beta = \{1, 2, 4, 13\}$
- $L = \{50, 100, 200\}$
- $\tau_0 = 0.33T_b = 1218$ ns

Fig. 5.1 shows (a) the bias bias($\hat{\tau}_0$) vs. SNR and (b) the variance var($\hat{\tau}_0$) vs. SNR for the TOA estimation for the case of $L = 50$ without interpolation. The CRB calculated for $\beta = 1$ with the expression from (4.11), which assumes uncorrelated noise, is included as a reference in dashed lines.

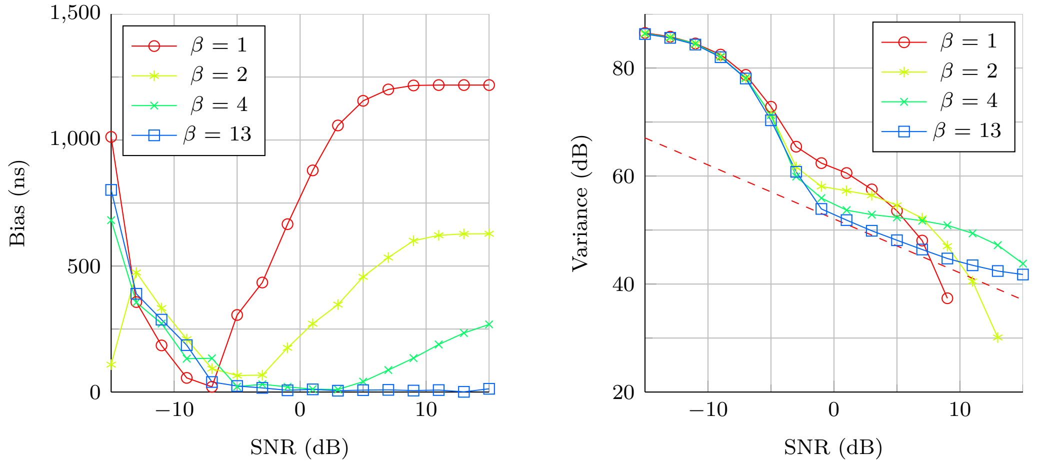

(a) bias($\hat{\tau}_0$) vs. SNR for different β values and $L = 50$.

(b) var($\hat{\tau}_0$) vs. SNR for different β values and $L = 50$.

Figure 5.1: Simulation results for the TOA estimation of a pure delay in LOS conditions for different sampling rates and without interpolation.

Fig. 5.1 (a) shows that, as the SNR increases, the bias tends to a constant term for the different values of β. This constant term is the minimum possible bias and it depends on the distance between the nearest sample and the delay τ_0. Since no interpolator is used, the delay estimate is $\hat{\tau}_0 = \hat{k}_0 \frac{T_b}{\beta}$, so a higher β improves the resolution and reduces the bias. Although apparently for $\beta = 13$ the bias is zero, the distance between τ_0 and the closest sample is not zero, thus the bias still reaches a constant value but at a higher SNR.

The variance plot in Fig. 5.1 (b) shows that an increase in SNR reduces the variance for all β. However, for lower values of β the variance tends to zero after a certain SNR is reached and we cannot evaluate the performance of the estimator by comparing its variance to the CRB. This is due to the low resolution, which causes the estimator to always return the same value once the SNR is high enough, thus having zero variance. An increase of the sampling rate divides the delay estimates into smaller intervals, improving the resolution and making the variance tend to zero at a higher SNR value. This effect is illustrated in Fig. 5.2, where $\hat{\tau}_0$ is assumed to be a discrete random Gaussian variable and its probability mass function (PMF) is represented as an example. As the figure shows, when the SNR is high enough the PMF is concentrated on a single value and the variance is zero. Increasing the sampling rate approximates the PMF to that of a continuous variable, up to the point where with $\beta \to \infty$ we have the continuous PDF.

Both bias and variance results show that a high resolution is required to reduce the bias and to be able to evaluate the variance of the estimator. Since in GSM the received signals are not sampled at very high rates, we will use the interpolator to determine if the resolution can be improved while still maintaining a low sampling rate.

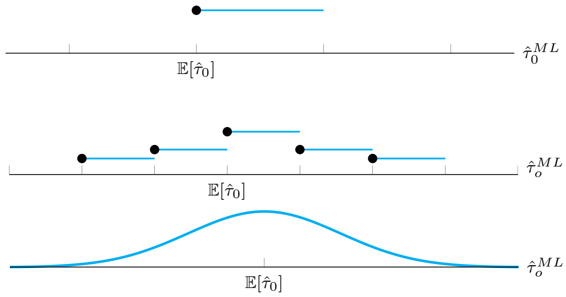

Figure 5.2: Effect of the sampling rate on the PMF of a discrete Gaussian random variable.

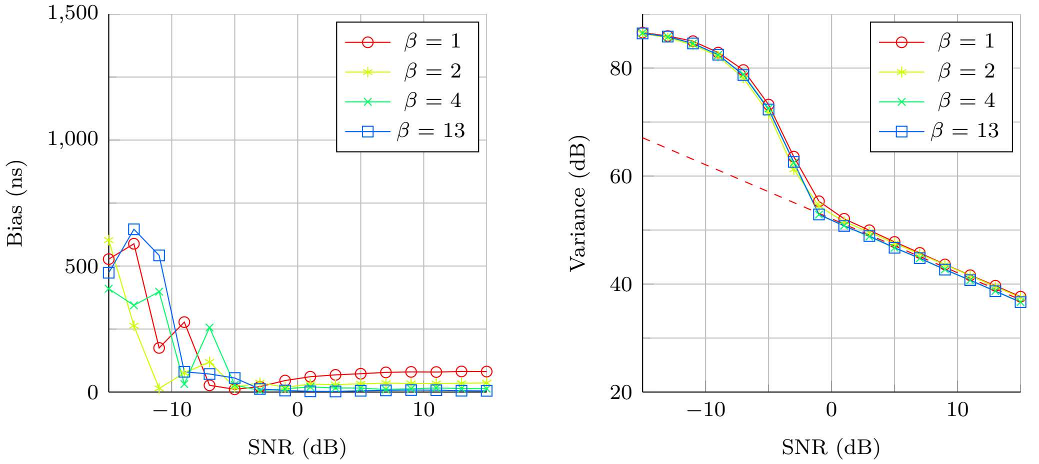

(a) bias($\hat{\tau}_0$) vs. SNR for different β values and $L = 50$.

(b) var($\hat{\tau}_0$) vs. SNR for different β values and $L = 50$.

Figure 5.3: Simulation results for the TOA estimation of a pure delay in LOS conditions and with interpolation for different sampling rates.

Fig. 5.3 shows the results for the TOA estimator when an interpolation function is used for different values of β and $L = 50$. First, the impact of the interpolation is clear comparing the plots in Fig. 5.1 and Fig. 5.3; the bias is significantly reduced and the variance no longer tends to zero and follows the trend of the CRB. We also observe that for all β the bias starts to converge to its final value at the same SNR where the variance converges to the CRB. Still, the use of an interpolator is not enough to reduce the bias to zero, although for $\beta = \{4, 13\}$ it is very close. With larger sampling rates the bias would eventually reach zero, since with a higher resolution the interpolator is able to estimate the real peak of the cross correlation more accurately and, therefore, reduce the bias. On the other hand, the variance shows a very small improvement when the sampling rate is increased. Even though with more samples the available information is increased, the variance curves converge to or are slightly above the CRB calculated for $\beta = 1$. Because of the noise correlation, when the sampling rate is increased the noise power also rises and the variance remains unchanged. This effect is explained in detail in Appendix B.

Regarding the length of the training sequence L, Fig. 5.4 shows the bias and variance for different L and a sampling rate equal to the Nyquist rate, i.e., $\beta = 2$. We observe from Fig. 5.4 (a) that the bias is not improved, although for higher values of L it reaches a constant value at a lower SNR. Moreover, from Fig. 5.4 (b) we can see that longer training sequences yield a better variance and, as expected, the performance for each curve is improved with increasing SNR. For instance, each time the training sequence length is doubled, the variance decreases by an amount of 3 dB. Also note that, as L is increased, the variance converges earlier to the CRB.

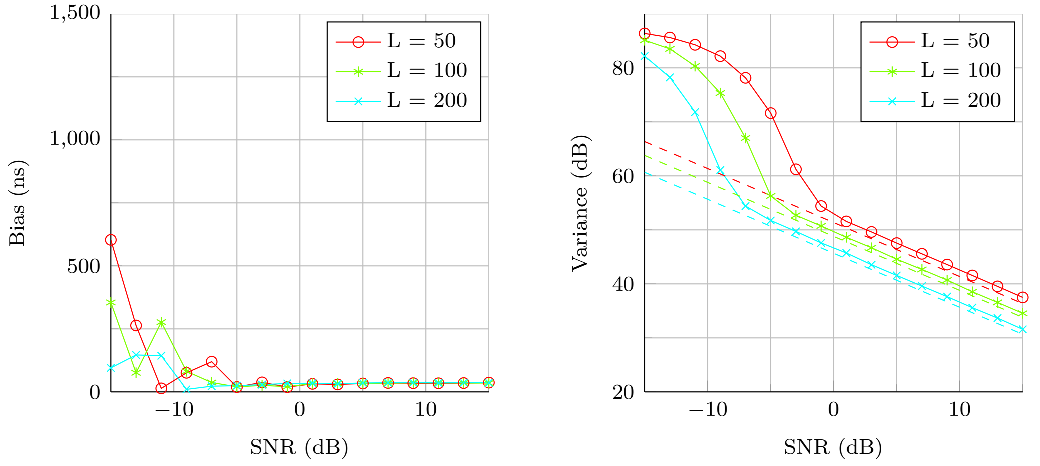

(a) bias($\hat{\tau}_0$) vs. SNR for different L values and $\beta = 2$.

(b) var($\hat{\tau}_0$) vs. SNR for different L values and $\beta = 2$.

Figure 5.4: Simulation results for the TOA estimation of a pure delay in LOS conditions and with interpolation for different training sequence lengths.

We can conclude that the use of the ML estimator in ideal LOS conditions is adequate. Although the estimator is biased, the bias can be reduced to zero simply by increasing the sampling rate. However, a higher sampling rate does not provide any noticeable benefit in terms of variance. Still, the variance of the estimator converges to the CRB, thus achieving the minimum possible variance. We also observe that a minimum SNR is required for the bias and the variance to converge to a constant and the CRB respectively. Below this SNR, the variance grows very large and the bias is seemingly random, so the results for the lower SNR cannot be used to estimate the performance of the TOA estimator in a real implementation. A longer training sequence lowers the minimum SNR requirement, hence allowing us to better predict the estimation performance at low SNR values, while also lowering the estimation variance.

5.2.2 Simulation results combining two slots in ideal LOS conditions

For the TOA estimation combining two slots explained in section 4.4, the log-likelihood function to be maximized in (4.33) is evaluated for a range of values of τ and δ. Fig. 5.5 depicts a realization of this process prior to the interpolation. As it can be seen, the output from the second correlator is shifted a number of samples for each value of δ. When the position of the two cross correlation functions coincides, the summation reaches its maximum value. The position of this maximum gives the estimates $\hat{\tau}_0$ and $\hat{\Delta}$ before the interpolation.

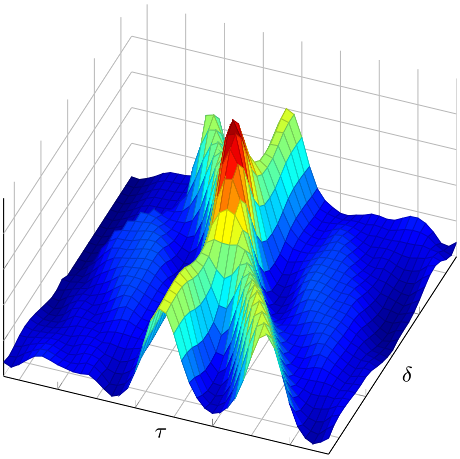

Figure 5.5: Visualization of the 2D log-likelihood function.

For the simulations combining two slots, the following sets of parameter values are chosen

- $\beta = 2$
- $L = 50$
- $\tau_0 = 0.33T_b = 1218$ ns
- $\Delta = 0.7T_b$=2584.4 ns

where Δ is the relative delay of the signals from the two slots.

Fig. 5.6 shows a comparison between the simulation results for one and two slots at a sampling rate β=2 with interpolation and an ideal LOS channel. We observe that, although the signal from the second slot has an additional relative bias Δ, the bias of $\hat{\tau}_0$

is not increased when combining two slots. This is a convenient result, as it means that the relative delay is estimated correctly. Moreover, the bias should remain unchanged when a second slot is added since the same cross correlation function is applied to the two slots and the channel does not change from slot to slot.

On the other hand, it can be observed that the variance is not reduced when combining the information from two slots. We would expect that, since the available information is doubled, the variance values should be halved. However, this does not happen because the need to estimate an additional parameter also increases the variance. Moreover, since Δ is estimated with the same method as τ_0, that is, maximizing the output of a correlator, their variances are equal. Consequently, although the addition of a second training sequence from another slot lowers the variance by 3 dB, the variance is also increased by 3 dB due to the estimation of Δ. As a result, the combination of two slots does not provide any benefit.

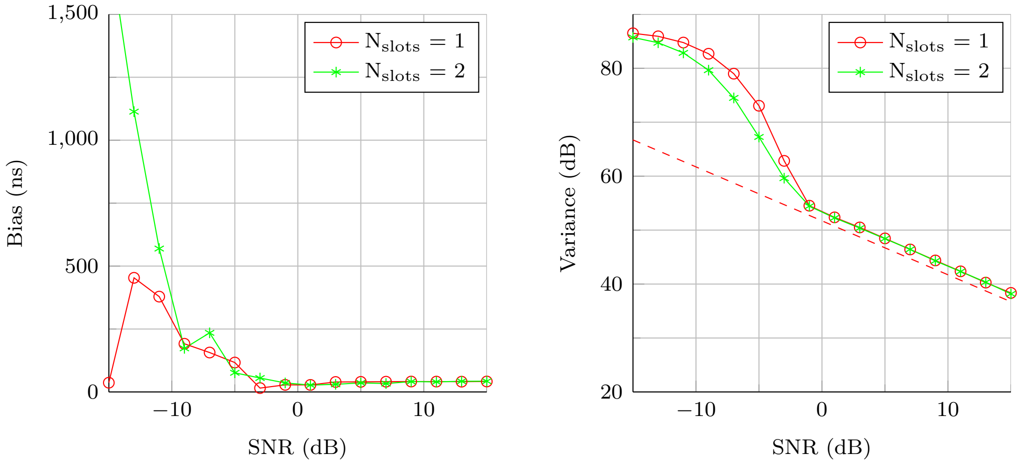

(a) bias($\hat{\tau}_0$) vs. SNR for different numbers of slots, $\beta = 2$ and $L = 50$.

(b) var($\hat{\tau}_0$) vs. SNR for different numbers of slots, $\beta = 2$ and $L = 50$.

Figure 5.6: Simulation results for the TOA estimation of a pure delay in LOS conditions for different numbers of slots and with interpolation.

5.2.3 Simulation results with the debris channel model

With the debris channel model, the parameter values considered for the sampling rate and the length of the random training sequence are the same as in the simulations in LOS conditions with a single slot so that we can observe the differences in the performance of the estimator caused by the debris channel. The considered parameter values are the following

- $\beta = \{1, 2, 4, 13\}$

- $L = \{50, 100, 200\}$
- multipath channel with 10 replicas
- $\tau_0 = 120$ ns

where τ_0 corresponds to the delay of the first arrival path. For the channel model, we consider the realization with CIR depicted in Fig. 3.7 and with parameters given in Table 3.2. In the generation of this channel, the distance between the transmitter and the receiver was set to 33 m, so the propagation delay in LOS conditions is 100 ns. Therefore, any estimation of the delay τ_0 will have an additional bias of 20 ns with respect to the LOS propagation delay. However, since it is not possible to estimate the LOS delay in a NLOS scenario, the bias is calculated with respect to the first path.

Fig. 5.7 shows the results for the TOA estimator considering the realistic model of the debris channel. The plots show the bias and the variance as functions of the SNR using different sampling rates β in (a) and (b), and different training sequence lengths L in (c) and (d). As before, for different sampling rates the training sequence length is $L = 50$, whereas for different training sequence lengths the sampling rate is $\beta = 2$.

The bias plot in Fig. 5.7 (a) shows that the estimator is biased for all the values of β and that the bias is reduced as β increases. However, the bias cannot be reduced to zero by increasing the sampling rate due to the NLOS and multipath propagation conditions of the debris channel. Because there is no line of sight, the first component is highly attenuated and not always the one with highest power. In such condition, since the TOA estimator finds the delay that maximizes the cross correlation, the first arrival will not be estimated in general. Still, even if the first path carried the most power, the different multipath components cannot be resolved at the receiver because of the low bandwidth of the GSM link and, consequently, the first arrival cannot be estimated accurately.

As in the case of an ideal channel, we observe from Fig. 5.7 (b) that increasing the sampling rate does not improve the variance due to the correlated noise. As expected, longer training sequences yield a better variance, as it can be seen from Fig. 5.7 (d). Again, each time the training sequence length is doubled, the variance decreases by an amount of 3 dB. We also observe from Fig. 5.7 (c) that a higher L does not alter the bias since the length of the training sequence does not affect the resolution of the estimator.

The simulation results show that the multipath propagation in the debris channel produces a large bias in the TOA estimation, while the variance remains unchanged if compared to the obtained results in an ideal LOS channel. In our scenario, a small error can be very significative because, due to the short distance between the MT and the FAP, the propagation delays we wish to estimate are very small. From the simulation results, a bias of 94 ns for $\beta = 13$ plus the 20 ns due to the NLOS propagation results in a total bias of 114 ns with respect to the propagation delay in LOS conditions. This bias translates into an error of 34.2 m, which is too large for the applications considered in this work.

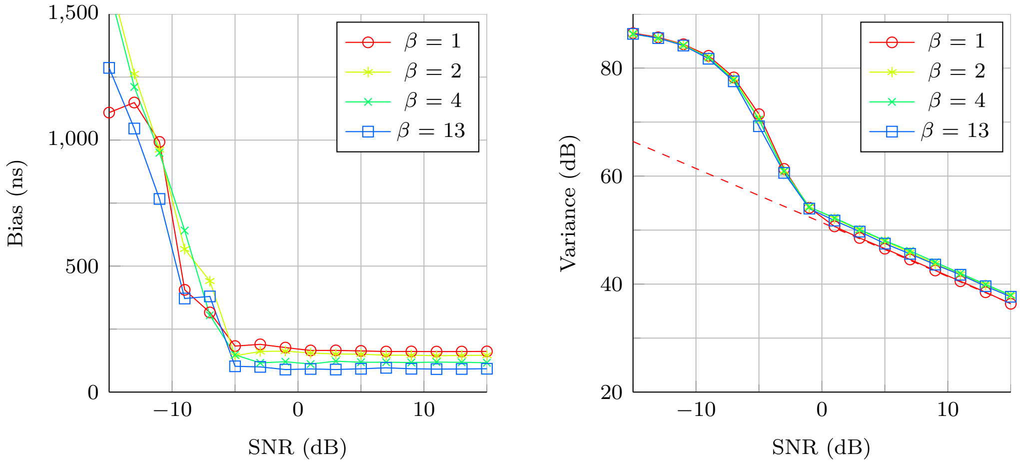

(a) bias($\hat{\tau}_0$) vs. SNR for different β values and $L = 50$.

(b) var($\hat{\tau}_0$) vs. SNR for different β values and $L = 50$.

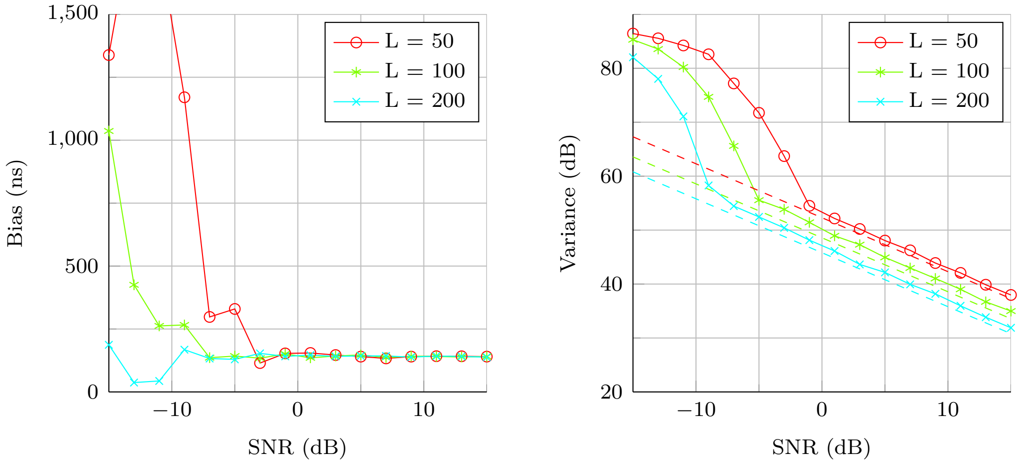

(c) bias($\hat{\tau}_0$) vs. SNR for different L values and $\beta = 2$.

(d) var($\hat{\tau}_0$) vs. SNR for different L values and $\beta = 2$.

Figure 5.7: Simulation results for the TOA estimation assuming the debris channel model and with interpolation.

5.2.4 Simulation results with the debris channel and a normal burst

In the previous simulations we studied how the type of channel, the SNR and the length of the training sequence and sampling rate affect the estimation accuracy. In a real implementation of the GSM link, an unmodified phone cannot transmit data sequences of arbitrary length and is restricted to the transmission of random access and normal bursts. Of these two types of bursts, we chose the normal burst since it is the most adequate for positioning purposes. However, only the central bits of the normal burst belonging to the training sequence are known at the receiver and, therefore, only these bits can be correlated with the received burst. With the simulations with a normal burst, our objective is to assess how the transmission of a burst in which the training sequence is located in between large data fields degrades the estimation performance.

For the simulations with a normal burst, the sampling rate is $\beta = 2$ and the realization of the debris channel is the same used in the previous simulations, with parameters given in Table 3.2. The length of the training sequence in a normal burst is $L = 26$ bits and the total length of the burst is 148 bits. Since the estimator correlates a copy of the training sequence with the received normal burst, it will estimate the position of the training sequence within the burst. The training sequence in the normal burst is located after the first 61 bits, so the delay to be estimated is $\tau_{train} = 61T_b + \tau_0$.

Figs. 5.8 (a) and (b) show a comparison of the bias and variance for a 26 bit random training sequence and a 148 bit burst. The CRB in the variance plot is calculated for a training sequence length $L = 26$. The bias plot in (a) shows that with a normal burst the bias is reduced. The bias varies because, once modulated, the training sequence within the normal burst and the local copy of the training sequence differ. In a GMSK modulation, the phase of a symbol depends on the phases of the previously transmitted symbols. Since in a normal burst there are 61 random bits prior to the training sequence, the modulation of the training sequence will begin with a random phase in each realization. Therefore, when the received burst is correlated with the local sequence, the delay of the correlation peak will have an additional random bias due to the modulation mismatch. Since the initial phase of the stored training sequence is 0, when the accumulated phase at the beginning of the training sequence in the burst is a multiple of 2π both sequences

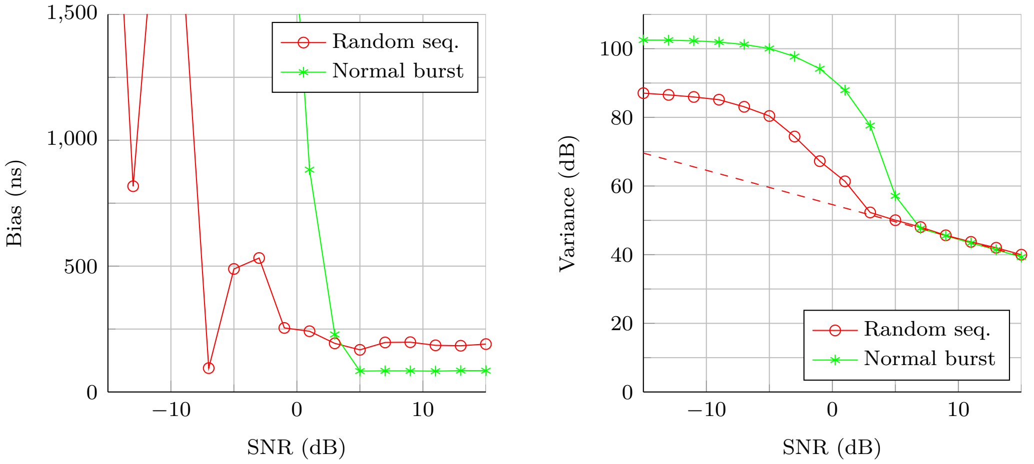

(a) bias($\hat{A}$) vs. SNR for different burst types. (b) var($\hat{A}$) vs. SNR for different burst types.

Figure 5.8: Simulation results for the TOA estimation with a random training sequence and a normal burst in multipath propagation conditions.

will have the same modulated waveform. On the variance plot in Fig. 5.8 (b), we observe that the variance with a normal burst is much higher until both curves converge to the CRB. This rise in variance is due to the fact that the training sequence is not completely uncorrelated with the rest of the burst, which causes numerous secondary peaks in the correlation function that interfere with the estimation.

To illustrate this effect, Fig. 5.9 (a) shows the autocorrelation function of a 26 bit random training sequence, and Fig. 5.9 (b) shows the cross correlation between a noiseless normal burst and the 26 bit training sequence. Clearly, it will be more difficult to estimate the correlation peak in (b) once the signal passes through the multipath channel and noise is added. Another drawback of using a normal burst is that, due to the increase in variance, a higher SNR is needed for both bias and variance to converge to their final trends.

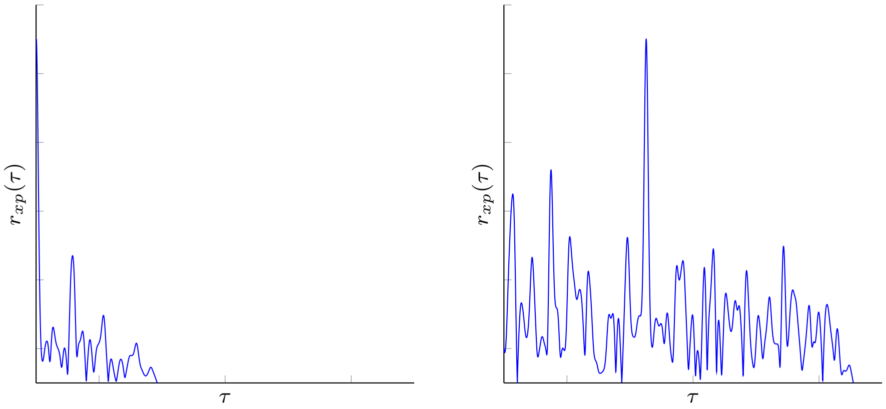

(a) Autocorrelation of a random 26 bit training sequence.

(b) Cross correlation of the normal burst with the 26 bit training sequence.

Figure 5.9: Comparison of the autocorrelation of a random training sequence with the cross correlation of a normal burst with its training sequence.

5.3 Challenges in the estimation of the first arrival in the debris channel

The simulation results show that, while the TOA estimator is able to accurately estimate the delay in a LOS channel, the multipath propagation in the debris channel causes a large bias. Ideally, we would be able to minimize the error if, instead of finding the maximum at the output of the correlator, the estimator detected the different multipath components and estimated the delay of the first one. With this purpose, other methods specifically designed for the detection of the first arrival in a multipath channel were considered. Particularly, a modified version of the high-resolution TOA detection method proposed in [22] was implemented. However, we were unable to achieve satisfactory results.

Due to the limited bandwidth of the GSM system, the different multipath components become unresolvable at the receiver and the TOA estimation algorithms are unable to detect the first arrival. Specifically, the flat fading and the lowpass filtering cause the multipath components to appear as one at the receiver while, in the case of the ML estimator, the correlator also makes the paths indistinguishable at its output.

In a flat fading channel the received signal $x(t)$ has the same value for all the delays τ_n, thus all the different paths can be considered as a single path with delay τ. With a delay spread of 118 ns for the CIR used in the simulations, the signal bandwidth would have to be $B >> \frac{1}{T_m} = 8.47$ MHz for the system not to be affected by the flat fading.

The lowpass filter at the receiver makes the paths unresolvable by expanding the time duration of the various multipath components, which reduces the time domain resolution. In a standard receiver, the signal at the input of the ADC is the received signal plus the noise convolved with the impulse response of the lowpass filter:

$$x(t) = (s_r(t) + \omega(t)) * b(t) = \frac{1}{2}u(t) * h_c(t) * b(t) + \omega(t) * b(t), \tag{5.1}$$

where $b(t)$ is an ideal lowpass filter with temporal and frequency responses

$$b(t) = \operatorname{sinc}(B_p t) \tag{5.2}$$

$$B(f) = \begin{cases} 1 & -\frac{B_p}{2} < f < \frac{B_p}{2} \\ 0 & \text{else} \end{cases} \tag{5.3}$$

If the channel $h_c(t)$ is a time invariant multipath channel as the one defined in (3.28), the result of its convolution with $b(t)$ is a summation of delayed, scaled and phase shifted sinc functions:

$$h_c(t) * b(t) = \sum_{n=0}^{P} \alpha_n e^{-j\phi_n} \operatorname{sinc}(B_p(t - \tau_n)). \tag{5.4}$$

So, the deltas in the CIR become sinc functions with a main lobe width equal to $\frac{1}{B_p}$. This causes a resolution loss in narrowband systems where the separation between multipath components is smaller than inverse of the filter bandwidth. Figure 5.10 shows the magnitude of the CIR used in the simulations before and after the lowpass filtering. As it can be observed, the multipath components are combined due to the widening caused by the filter. For the paths to be resolvable at the output of the filter, the time response of the filter must have a -3 dB width smaller than the separation between the multipath components. In our scenario, this would require a filter bandwidth of tens of MHz.

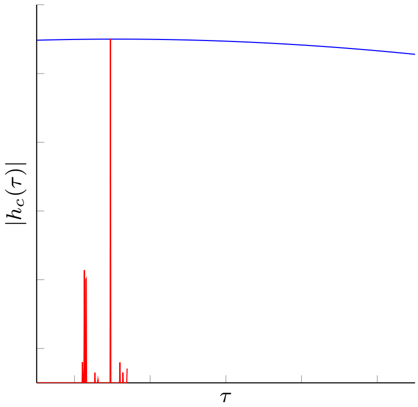

Figure 5.10: Magnitude of the CIR of the debris channel before (red) and after (blue) the lowpass filter.

The correlator in the ML estimator also makes it difficult to differentiate the multiple paths at its output. Since the received signal is a sum of copies of the original transmitted signal, the output of the correlator is a sum of delayed autocorrelation functions. As a result, the ability of the estimator to detect the individual multipath components depends on the width of the autocorrelation functions, which is inversely proportional to the signal bandwidth, and the separation of the multipath components. The width of the autocorrelation functions. If the path separation is larger than the -3 dB width of the autocorrelation, then the individual correlation peaks will be identifiable. For instance, the -3 dB width of the 50 bit training sequences used in the simulator is approximately two bit periods, that is 7384 ns. With path separations of tens of nanoseconds in the debris channel (Table 3.2), it is clearly not possible to detect the individual correlation peaks at the output of the correlator.

We can conclude that, given the specifications of the GSM link, it is not possible to accurately estimate the delay of the first arrival τ_0 with the proposed ML estimator. Even if we had formulated the TOA estimator for the multipath case, the flat fading and the lowpass filtering already make the paths unresolvable, thus the TOA estimator would only detect a single path. For instance, Fig. 5.11 (a) shows the output of the correlator for a 50 bit random training sequence with a resolution of 1 ns when no Gaussian noise is added to the received signal, and Fig. 5.11 (b) shows a zoomed view of the correlation peak in blue with the magnitude of the of the CIR represented in red. As it can be observed, there is only a single correlation peak and it does not coincide with any multipath component. This peak is the result of the grouping of the multipath components caused by the fading and the filter, and it has a delay τ_0' that can take any value in the range $[\tau_0, \tau_0 + T_m]$. Since the TOA estimator finds the delay that maximizes the cross correlation, it will estimate the delay of this peak. The final TOA estimation is the propagation time in LOS conditions plus the error caused by the delay spread, the NLOS propagation, the noise and the estimator itself:

$$\hat{\tau}_0 = \tau_{0_{LOS}} + \varepsilon_{NLOS} + \varepsilon_{T_m} + \varepsilon_{\omega} + \varepsilon_{est} \tag{5.5}$$

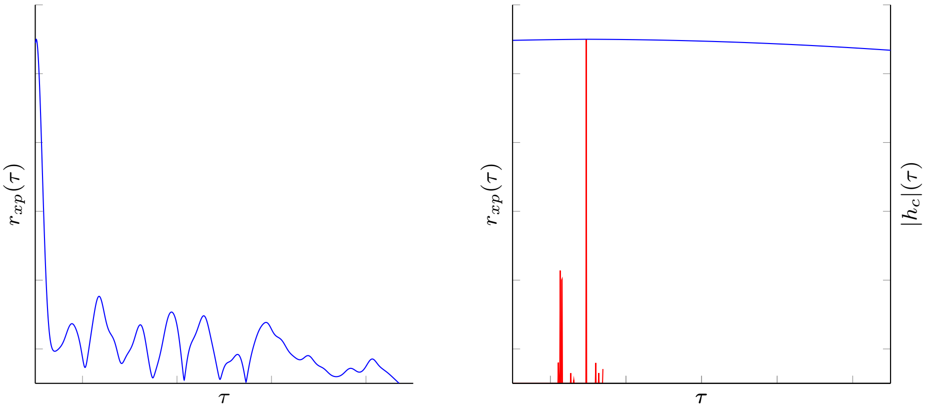

(a) Complete correlator output.

(b) Zoomed view of the correlation peak (blue) and magnitude of the debris CIR (red).

Figure 5.11: Correlator output for a 50 bit random sequence with a resolution of 1 ns.

5.4 Simulation results of the ML amplitude estimator

With the amplitude estimation we are able to determine the strength of the signal after it passes through the wireless channel, and the SNR at the receiver. The SNR can be used to obtain the expected accuracy of the TOA estimator using the performance plots presented in the previous sections of this chapter. In this section we analyze the performance of the ML amplitude estimator given in (4.16) in the case of the debris channel and the transmission of a random training sequence and a normal burst. The performance metrics for the simulations are the bias and the variance, computed from 10000 independent realizations and given respectively by

$$\text{bias}(\hat{A}) = \left|\mathbb{E}[\hat{A} - A]\right|, \qquad \text{var}(\hat{A}) = 10\log_{10}(\mathbb{E}[|\hat{A} - \mathbb{E}[\hat{A}]|^2])$$

where A is the reference amplitude and $\hat{A}$ is the estimated amplitude. The reference amplitude A is calculated by the link simulator as the average amplitude of the received burst before the addition of noise. Given that the amplitude estimator requires the delay of the received signal as a parameter in order to obtain $\hat{A}$, in each realization the delay is estimated using the ML TOA estimator and then passed to the ML amplitude estimator for the estimation.

For the simulations with the debris and a random training sequence, the following parameter values are considered

- $\beta = \{1, 2, 4, 13\}$
- $L = \{50, 100, 200\}$
- multipath channel with 10 replicas
- $A = 0.637$ mV

The realistic channel model is the same as before, i.e., a random realization with CIR depicted in Fig. 3.7 and with the parameters given in Table 3.2.

Fig. 5.12 shows the simulation results for the amplitude estimation. The plots show the bias and variance for different values of β in (a) and (b), and the corresponding curves for the case of different training sequence lengths L in (c) and (d). For different sampling rates the training sequence length is $L = 50$, whereas for different training sequence lengths the sampling rate is $\beta = 2$. The CRB for $\beta = 1$ with uncorrelated noise is included as a reference in dashed lines.

From Fig. 5.12 (a) we observe that the bias approaches a constant as the SNR increases and that an increase of β yields a reduction of the bias. The variance curves in Fig. 5.12 (b) exhibit the same performance for all values of β, approaching the theoretical limits for the case of $\beta = 1$. As in the TOA estimation, the variance of the amplitude estimation cannot be reduced by increasing the sampling rate due to the correlation of the Gaussian noise, which causes the signal power and the noise power to grow in the same proportion when the sampling rate is increased.

Regarding the training sequence length, in Figs. 5.12 (c) and (d) we observe that a higher L does not reduce the bias, while the variance is reduced by 3 dB each time the sequence length is doubled. Moreover, with an increase in length both bias and variance converge earlier to their final trends.

For the simulations with a normal burst a sampling rate $\beta = 2$ was chosen. Figs. 5.13 (a) and (b) show the bias and variance of the amplitude estimator when a random sequence and a normal burst are used. We observe in (a) that, unlike in the TOA estimation, the modulation differences between the training sequence in the normal burst and the local training sequence do not impact on the bias. On the other hand, the variance plot in (b) shows that with a normal burst the variance is higher than with a random burst until both curves approach the CRB and follow its trend.

The simulation results for the ML amplitude estimator show that, with an error as small as 0.004 mV in the worst case, it is able to estimate the amplitude of the received burst with high accuracy, and also that the estimation variance is close to the benchmark set by the CRB. As in the TOA estimation results, a minimum SNR is required for both bias and variance to converge, thus the results obtained for the lower SNR values cannot be used to predict the performance of the estimator. On the other hand, the use of a normal burst does not increase the estimation error, although it produces a slight rise in the variance and the minimum required SNR.

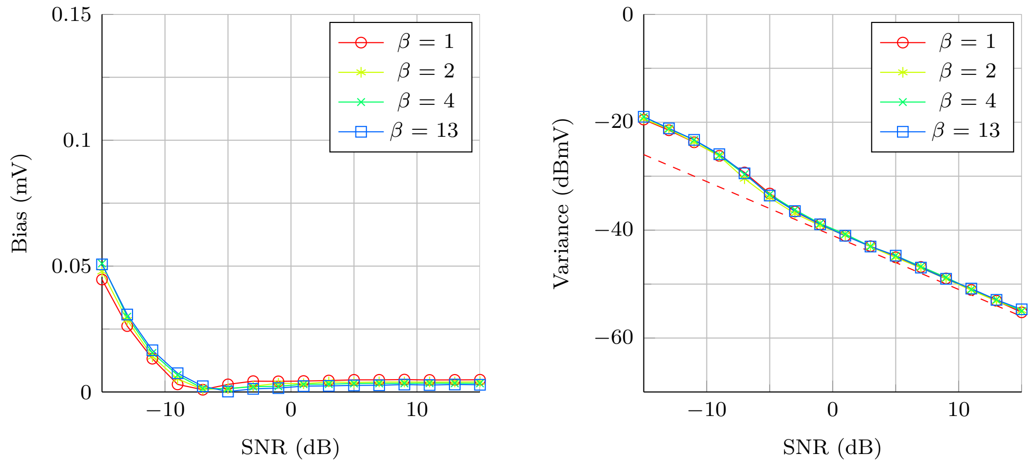

(a) bias($\hat{A}$) vs. SNR for different β values and $L = 50$.

(b) var($\hat{A}$) vs. SNR for different β values and $L = 50$.

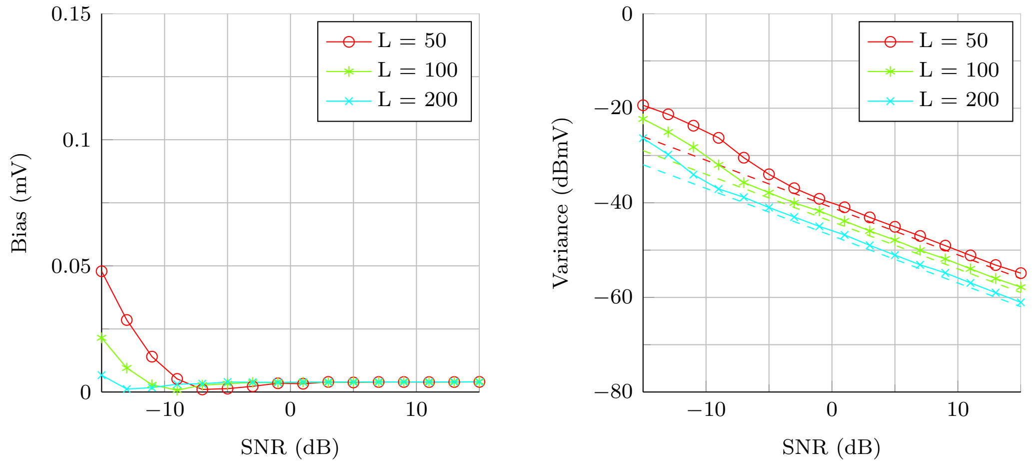

(c) bias($\hat{A}$) vs. SNR for different L values and $\beta = 2$.

(d) var($\hat{A}$) vs. SNR for different L values and $\beta = 2$.

Figure 5.12: Simulation results for the amplitude estimation in multipath propagation conditions.

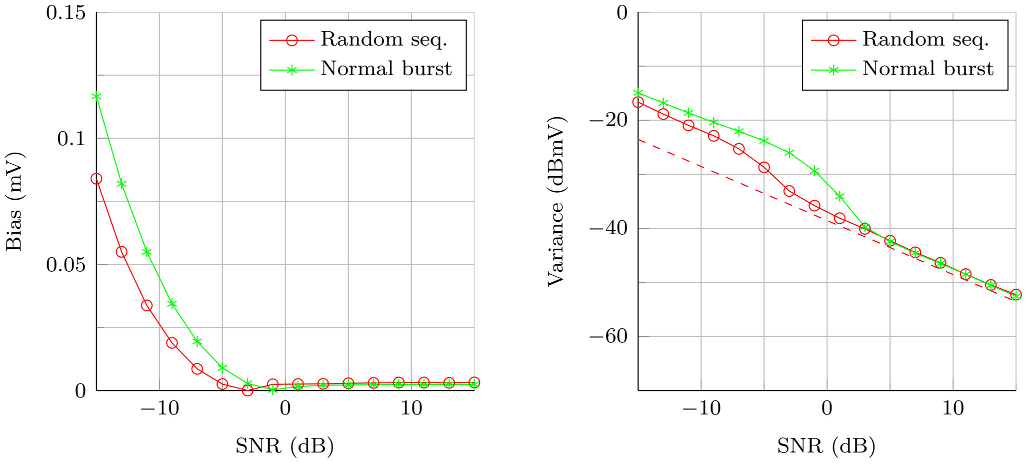

(a) bias($\hat{A}$) vs. SNR for different burst types.

(b) var($\hat{A}$) vs. SNR for different burst types.

Figure 5.13: Simulation results for the amplitude estimation for different burst types in multipath propagation conditions.

5.5 Conclusions of the simulation results

In the simulations we have characterized the performance of the TOA and amplitude estimators by calculating their bias and variance statistics. The TOA estimator has been evaluated in several scenarios which had different configurations such as the number of slots or the type of wireless channel. In these configurations, the impact of the sampling rate, the length of the burst and the type of burst has been studied. In general, the ML TOA estimator performs well in LOS conditions, although when the debris channel is introduced the estimation bias is significantly increased. As for the amplitude estimator, the simulations with the debris channel show that the estimations are very accurate.

With the ideal LOS channel, the simulations show that the ML TOA estimator is able to accurately estimate the delay of the received burst. With no interpolation the estimation bias is subject to the sampling period, while with an interpolator the estimation bias is close to zero for sampling rates above 2 samples per symbol. Therefore, unless the system is able to work at very high sampling rates, the use of an interpolator is mandatory. In the same LOS conditions, the TOA estimation combining the bursts from two slots has been tested. However, this method does not improve the estimation because of the need to estimate an additional parameter.

With the debris channel, the bias of the TOA estimator is originated by the NLOS and multipath propagation conditions. This bias is always positive, meaning that the MT seems to be further away than it is in reality. Although the bias from the NLOS is relatively small when compared to the bias from the multipath, it is an error that cannot be corrected since the estimator can only try to estimate the delay of the first arrival, which will always have an additional delay due to the NLOS. On the other hand, the bias from the multipath propagation causes an error comparable to the delays we wish to estimate, which results in a large error percentage. This error might be compensated if the ML estimator detected the first path instead of the maximum at the output of the correlator. However, with a delay spread of 118 ns for the realization of the debris channel used in the simulations, the multipath components are combined at the receiver and the estimator is unable to detect the individual paths. Several other techniques were considered to solve this problem but the results were not satisfactory and therefore not included in this work.

Regarding the estimation variance, the simulations show that the variance of both TOA and amplitude estimators is close to the Cramér-Rao bound from a certain SNR, thus we can confirm that we are close to the optimum performance. We observe in the simulations that a higher sampling rate does not reduce the variance and that it can only be improved by increasing the length of the training sequence. As a rule of thumb, each time the length is doubled the variance decreases 3 dB. On the other hand, a sampling rate $\beta > 1$ does not provide any noticeable benefit in terms of variance because of the correlation of the Gaussian noise. Although with a higher sampling rate the available information is increased, the noise power increases in the same proportion and the variance is not reduced. However, the noise model used in this work could be too pessimistic and in a real situation it might not be as correlated and some benefit might be obtained from having a sampling rate higher than one sample per symbol.

Additionally, it is observed that when a normal burst is transmitted, which would be the case in a real implementation, the variance of the TOA estimator also reaches the CRB but at a higher SNR because the data fields next to the training sequence produce secondary peaks at the output of the correlator that interfere with the estimation. Moreover the bias varies because of the differences between the received training sequence and the local copy. In the case of the amplitude estimator, the use of a normal burst does not modify the bias, although the variance is increased.

Chapter 6

Conclusions

This thesis has addressed the problem of estimating the TOA and RSS of a signal transmitted from a mobile terminal in a disaster scenario where the terminal is buried under the debris from a collapsed building. An accurate estimation of the two parameters is crucial for a successful implementation of the RESCUECELL system, a GSM-based local network dedicated to the localization of buried people in emergency situations. The results derived from this work contribute towards the design of the RESCUECELL system and help anticipate the problems we might encounter in a real implementation.

Throughout the chapters in this thesis we described the process that lead to the implementation of the link simulator and the simulation results. In Chapter 2 we reviewed the positioning methods available in the GSM network and considered that the TDOA method was the most adequate for our purposes due to its higher accuracy and compatibility with all MT. However, the TOA and RSS measurements provided by the GSM network are not accurate enough, so custom measurement techniques needed to be developed. In Chapter 3 we introduced the simulator of the communication link between the MT and the FAP, and described he models and the implementation of the transmitter, the channel and the receiver. The realistic model of the debris channel is especially important, since it allows us to accurately reproduce the conditions of a disaster scenario. In Chapter 4, we proposed the maximum likelihood estimators for the TOA and amplitude and derived the Cramér-Rao bounds. Finally, in Chapter 5 we presented the simulation results in several scenarios and analyzed the impact of the different parameters.

The simulation results with the debris channel show that, while the amplitude estimation is highly accurate, the TOA estimation has a large error due to the NLOS and multipath propagation. Highly resolutive techniques for the estimation of the first arrival have been studied and implemented, although the results were not satisfactory. Since the paths become unresolvable because of the low bandwidth of the GSM system, the TOA estimators are unable to detect the first arrival. Hence, since the system bandwidth cannot be modified, future efforts should be focused on reducing the variance of the estimates. Moreover, data fusion algorithms can be implemented to combine the measurements from different slots or FAPs at the control center and reduce the estimation bias.

The results from the simulations serve as reference for the design of the FAP specifications. There are three parameters which can be adjusted to improve the performance of the estimators: the SNR, the length of the training sequence and the sampling rate. A minimum SNR is required in order to ensure a constant average bias and a variance that is close to the CRB. This requirement for a minimum SNR can be lowered by using a longer training sequence, which in turn also yields a reduced variance. In the simulations we observe that when a normal burst is transmitted, the variance is much higher because the bits that do not belong to the training sequence interfere with the estimation. Hence, we recommend that the FAP should be able to use the complete normal burst as a training sequence for the estimation process. This would increase the training sequence length from 26 to 148 bits, which results in a variance reduction of approximately 7.5 dB. On the other hand, a high sampling rate is not necessary because, thanks to the interpolator, the bias introduced by the estimator itself is kept to a minimum. Moreover, due to the noise correlation, a higher sampling rate does not reduce the variance. Still, the use of a sampling rate as high as the hardware allows is recommended since in a real implementation the noise might not be as correlated and a reduction in variance might be achieved.

The next step in the RESCUECELL project is the implementation of a system-level simulator that includes multiple FAPs and the CC to investigate the performance of the TDOA positioning method. Although not included in this work, the bias and variance statistics for a large number of different realizations of the debris were also generated with the link simulator. These statistics will be used in the system simulator to reproduce the TOA and amplitude measurements performed at the different FAPs of the network, which will then be used for the TDOA localization.

Appendices

Appendix A

CRB for the TOA and amplitude estimators

Given a known random vector $\mathbf{x}$ that depends on a set of parameters $\boldsymbol{\theta} = \{\theta_1, \theta_2 \cdots \theta_N\}$, the CRB formula states that the minimum variance with which an unbiased estimator can estimate an unknown parameter $\theta_i \in \{\theta_1, \theta_2, \cdots, \theta_N\}$ of the probability density function $f_{\mathbf{x}}(\mathbf{x})$ is

$$\sigma^2_{\hat{\theta}_i} \geq (\mathbf{F}^{-1})_{ii}, \tag{A.1}$$

where $\mathbf{F}$ is an $N \times N$ matrix known as the Fisher Information Matrix (FIM). The entries of the FIM are a measure of the amount of information that the vector $\mathbf{x}$ holds about the unknown parameters $\boldsymbol{\theta}$, and are defined as

$$F_{ij} = \mathbb{E}[-\frac{\partial^2}{\partial\theta_i \partial\theta_j} \ln f_{\mathbf{x}}(\mathbf{x}|\boldsymbol{\theta})], \tag{A.2}$$

where $\ln f_{\mathbf{x}}(\mathbf{x}|\boldsymbol{\theta})$ is the so-called log-likelihood function of $\boldsymbol{\theta}$.

For the calculation of the CRB for the TOA and amplitude estimators, let us define the random vector $\mathbf{x}$ as the received sampled signal from section 4.1

$$\mathbf{x} = \mathbf{p}(\tau_0) + \boldsymbol{\omega}, \tag{A.3}$$

with log-likelihood function

$$\ln f_x(\mathbf{x}|\boldsymbol{\theta}) = -\ln\pi|\mathbf{R}_w| - (\mathbf{x} - A\mathbf{p}(\tau_0))^H \mathbf{R}_w^{-1} (\mathbf{x} - A\mathbf{p}(\tau_0)) \tag{A.4}$$

and unknown parameters $\boldsymbol{\theta} = \{A, \tau_0\}$.

First, we compute the partial derivatives of the log-likelihood function:

$$\frac{\partial \ln f_x(\mathbf{x}|\boldsymbol{\theta})}{\partial A^*} = \mathbf{p}^H(\tau_0)\mathbf{R}_w^{-1}\underbrace{(\mathbf{x} - A\mathbf{p}(\tau_0))}_{\boldsymbol{\omega}} \tag{A.5}$$

$$\frac{\partial^2 \ln f_x(\mathbf{x}|\boldsymbol{\theta})}{\partial A \partial A^*} = -\mathbf{p}^H(\tau_0)\mathbf{R}_w^{-1}\mathbf{p}(\tau_0) \tag{A.6}$$

$$\frac{\partial \ln f_x(\mathbf{x}|\boldsymbol{\theta})}{\partial \tau_0} = A^*\frac{\partial \mathbf{p}^H(\tau_0)}{\partial \tau_0}\mathbf{R}_w^{-1}(\mathbf{x} - A\mathbf{p}(\tau_0)) + A(\mathbf{x} - A\mathbf{p}(\tau_0))^H\mathbf{R}_w^{-1}\frac{\partial \mathbf{p}(\tau_0)}{\partial \tau_0} \tag{A.7}$$

$$\begin{aligned}\frac{\partial^2 \ln f_x(\mathbf{x}|\boldsymbol{\theta})}{\partial^2 \tau_0} &= A\frac{\partial^2 \mathbf{p}^H(\tau_0)}{\partial \tau_0^2}\mathbf{R}_w^{-1}(\mathbf{x} - A\mathbf{p}(\tau_0)) - |A|^2\frac{\partial \mathbf{p}^H(\tau_0)}{\partial \tau_0}\mathbf{R}_w^{-1}\frac{\partial \mathbf{p}(\tau_0)}{\partial \tau_0} \\ &- |A|^2\frac{\partial \mathbf{p}^H(\tau_0)}{\partial \tau_0}\mathbf{R}_w^{-1}\frac{\partial \mathbf{p}(\tau_0)}{\partial \tau_0} + A(\mathbf{x} - A\mathbf{p}(\tau_0))^H\mathbf{R}_w^{-1}\frac{\partial^2 \mathbf{p}(\tau_0)}{\partial \tau_0^2}\end{aligned} \tag{A.8}$$

$$\frac{\partial^2 \ln f_x(\mathbf{x}|\boldsymbol{\theta})}{\partial A^* \partial \tau_0} = \frac{\partial^2 \ln f_x(\mathbf{x}|\boldsymbol{\theta})}{\partial \tau_0 \partial A^*} = \frac{\partial \mathbf{p}^H(\tau_0)}{\partial \tau_0}\mathbf{R}_w^{-1}(\mathbf{x} - A\mathbf{p}(\tau_0)) - A\mathbf{p}(\tau_0)^H\mathbf{R}_w^{-1}\frac{\partial \mathbf{p}(\tau_0)}{\partial \tau_0} \tag{A.9}$$

$$\frac{\partial^2 \ln f_x(\mathbf{x}|\boldsymbol{\theta})}{\partial A \partial \tau_0} = \frac{\partial^2 \ln f_x(\mathbf{x}|\boldsymbol{\theta})}{\partial \tau_0 \partial A} = (\frac{\partial^2 \ln f_x(\mathbf{x}|\boldsymbol{\theta})}{\partial A^* \partial \tau_0})^H \tag{A.10}$$

Then, we calculate the entries of $\mathbf{F}$:

$$F_{11} = \mathbb{E}[-\frac{\partial^2 \ln f_x(\mathbf{x}|\boldsymbol{\theta})}{\partial A \partial A^*}] = \mathbf{p}^H(\tau_0)\mathbf{R}_w^{-1}\mathbf{p}(\tau_0) \tag{A.11}$$

$$F_{12} = \mathbb{E}[-\frac{\partial^2 \ln f_x(\mathbf{x}|\boldsymbol{\theta})}{\partial A^* \partial \tau_0}] = A\mathbf{p}^H(\tau_0)\mathbf{R}_w^{-1}\frac{\partial \mathbf{p}(\tau_0)}{\partial \tau_0} \tag{A.12}$$

$$F_{21} = \mathbb{E}[-\frac{\partial^2 \ln f_x(\mathbf{x}|\boldsymbol{\theta})}{\partial A \partial \tau_0}] = A^*\frac{\partial \mathbf{p}^H(\tau_0)}{\partial \tau_0}\mathbf{R}_w^{-1}\mathbf{p}^H(\tau_0) \tag{A.13}$$

$$F_{22} = \mathbb{E}[-\frac{\partial^2 \ln f_x(\mathbf{x}|\boldsymbol{\theta})}{\partial^2 \tau_0}] = 2|A|^2\frac{\partial \mathbf{p}^H(\tau_0)}{\partial \tau_0}\mathbf{R}_w^{-1}\frac{\partial \mathbf{p}(\tau_0)}{\partial \tau_0} \tag{A.14}$$

Finally, we obtain the inverse FIM as

$$\mathbf{F}^{-1} = \frac{1}{|\mathbf{F}|}\begin{bmatrix} F_{22} & -F_{21} \\ -F_{12} & F_{11} \end{bmatrix}, \tag{A.15}$$

where the determinant of $\mathbf{F}$ is

$$|\mathbf{F}| = 2|A|^2\mathbf{p}^H(\tau_0)\mathbf{R}_w^{-1}\mathbf{p}(\tau_0)\frac{\partial\mathbf{p}^H(\tau_0)}{\partial\tau_0}R_w^{-1}\frac{\partial\mathbf{p}(\tau_0)}{\partial\tau_0} - |A|^2|\mathbf{p}^H(\tau_0)\mathbf{R}_w^{-1}\frac{\partial\mathbf{p}(\tau_0)}{\partial\tau_0}|^2. \tag{A.16}$$

The CRBs for the unknown parameters A and τ_0 are

$$\begin{aligned}\sigma_{\hat{A}}^2 \geq (\mathbf{F}^{-1})_{11} = \frac{\mathbf{F}_{22}}{|\mathbf{F}|} &= \frac{2|A|^2\frac{\partial\mathbf{p}^H(\tau_0)}{\partial\tau_0}\mathbf{R}_w^{-1}\frac{\partial\mathbf{p}(\tau_0)}{\partial\tau_0}}{2|A|^2\mathbf{p}^H(\tau_0)\mathbf{R}_w^{-1}\mathbf{p}(\tau_0)\frac{\partial\mathbf{p}^H(\tau_0)}{\partial\tau_0}R_w^{-1}\frac{\partial\mathbf{p}(\tau_0)}{\partial\tau_0} - |A|^2\left|\mathbf{p}^H(\tau_0)\mathbf{R}_w^{-1}\frac{\partial\mathbf{p}(\tau_0)}{\partial\tau_0}\right|^2} \\ &= \frac{1}{\mathbf{p}^H(\tau_0)\mathbf{R}_w^{-1}\mathbf{p}(\tau_0) - \frac{1}{2}\frac{\left|\mathbf{p}^H(\tau_0)\mathbf{R}_w^{-1}\frac{\partial\mathbf{p}(\tau_0)}{\partial\tau_0}\right|^2}{\frac{\partial\mathbf{p}^H(\tau_0)}{\partial\tau_0}R_w^{-1}\frac{\partial\mathbf{p}(\tau_0)}{\partial\tau_0}}} \\ &= \frac{1}{\mathbf{p}^H(\tau_0)\mathbf{R}_w^{-1}\mathbf{p}(\tau_0) - \frac{1}{2}\frac{\left|\mathbf{p}^H(\tau_0)\mathbf{R}_w^{-1}\frac{\partial\mathbf{p}(\tau_0)}{\partial\tau_0}\right|^2}{\frac{\partial\mathbf{p}^H(\tau_0)}{\partial\tau_0}\mathbf{R}_w^{-1}\frac{\partial\mathbf{p}(\tau_0)}{\partial\tau_0}}} \end{aligned} \tag{A.17}$$

$$\begin{aligned}\sigma_{\hat{\tau}_0}^2 \geq (\mathbf{F}^{-1})_{22} = \frac{\mathbf{F}_{11}}{|\mathbf{F}|} &= \frac{\mathbf{p}^H(\tau_0)\mathbf{R}_w^{-1}\mathbf{p}(\tau_0)}{2|A|^2\mathbf{p}^H(\tau_0)\mathbf{R}_w^{-1}\mathbf{p}(\tau_0)\frac{\partial\mathbf{p}^H(\tau_0)}{\partial\tau_0}R_w^{-1}\frac{\partial\mathbf{p}(\tau_0)}{\partial\tau_0} - |A|^2\left|\mathbf{p}^H(\tau_0)\mathbf{R}_w^{-1}\frac{\partial\mathbf{p}(\tau_0)}{\partial\tau_0}\right|^2} \\ &= \frac{1}{2|A|^2\frac{\partial\mathbf{p}^H(\tau_0)}{\partial\tau_0}\mathbf{R}_w^{-1}\frac{\partial\mathbf{p}(\tau_0)}{\partial\tau_0} - \frac{|A|^2\ |\mathbf{p}^H(\tau_0)\mathbf{R}_w^{-1}\frac{\partial\mathbf{p}(\tau_0)}{\partial\tau_0}|^2}{\mathbf{p}^H(\tau_0)\mathbf{R}_w^{-1}\mathbf{p}(\tau_0)}} \end{aligned} \tag{A.18}$$

Appendix B

Effects of noise correlation in TOA and amplitude estimation

Although an increase of the sampling rate or the training sequence length brings more information available for the estimation, only a length increase results in a lower variance and faster convergence to the CRB. To explain this behaviour we will examine the signal-to-noise ratio SNR_c at the output of the correlator of the TOA estimator, and the variance of the amplitude estimator, both for a fixed delay $\tau = \tau_0$, a length of the training sequence L and a sampling rate β.

In the TOA estimator, an increase of SNR_c reduces the effect of the noise and, consequently, the variance of the estimation is also reduced. Knowing that the noise is a zero-mean random variable, the power at the output of the correlator is

$$\mathbb{E}[|\mathbf{x}^H \mathbf{p}(\tau_0)|^2] = \mathbb{E}[|A\mathbf{p}^H(\tau_0)\mathbf{p}(\tau_0) + \boldsymbol{\omega}^H \mathbf{p}(\tau_0)|^2] = |A|^2 \, ||\mathbf{p}||^4 + \mathbf{p}^H(\tau_0)\mathbf{R}_\omega \mathbf{p}(\tau_0), \quad \text{(B.1)}$$

where the first term corresponds to the signal power and the second term corresponds to the noise power. Since the GSM signals have a constant modulus equal to 1, the norm of the training sequence is $||\mathbf{p}||^2 = L\beta$. Dividing the signal power by the noise power, the resulting SNR expression is

$$SNR_c = \frac{(L\beta)^2 |A|^2}{\mathbf{p}^H(\tau_0)\mathbf{R}_\omega \mathbf{p}(\tau_0)}. \quad \text{(B.2)}$$

If the Gaussian noise were uncorrelated for any value of β, the SNR at the output of the correlator would be

$$SNR_c = \frac{(L\beta)^2 |A|^2}{\sum_{i=0}^{L\beta} |p_i|^2 \cdot r_\omega(i)} = \frac{(L\beta)^2 |A|^2}{L\beta \cdot r_\omega(0)} = L\beta \cdot SNR, \quad \text{(B.3)}$$

We see that under this assumption when the number of samples is increased, either by increasing the sequence length or the sampling rate, the signal power grows exponentially and the noise power grows linearly. Thus, a larger number of samples increases the signal power and reduces the influence of the noise, which results in a lower variance of the TOA estimation. However, this is not the case when the noise is correlated. With correlated noise, the SNR at the output of the correlator is

$$SNR_c = \frac{(L\beta)^2|A|^2}{\sum\limits_{i,l=0}^{L\beta} p_i^* \cdot p_l \cdot r_\omega(i-l)}. \tag{B.4}$$

Using the inverse discrete-time Fourier transform, we can write the noise power in (B.4) as

$$\begin{aligned}\sum_{i,l=0}^{L\beta} p_i^* \cdot p_l \cdot r_\omega(i-l) &= \sum_{i,l=0}^{L\beta} p_i^* \cdot p_l \cdot \int_{-\frac{1}{2}}^{\frac{1}{2}} S(f) e^{j2\pi f(i-l)}\, df \\ &= \int_{-\frac{1}{2}}^{\frac{1}{2}} S(f) \sum_{i=0}^{L\beta} p_i^* e^{j2\pi f i} \cdot \sum_{l=0}^{L\beta} p_l e^{-j2\pi f l}\, df \\ &= \int_{-\frac{1}{2}}^{\frac{1}{2}} S(f)|P(f)|^2\, df,\end{aligned} \tag{B.5}$$

where $S(f)$ is the power spectral density of the noise, defined as

$$S(f) = \mathscr{F}\{r_\omega(m)\} = \frac{2N_0\beta}{T_b}\Pi\left(\frac{f}{\frac{T_b \cdot B_p}{\beta}}\right). \tag{B.6}$$

Knowing that $\int |P(f)|^2 = \sum |p_i|^2 = L\beta$, if we substitute (B.6) into (B.5) and develop the resulting expression, we obtain

$$\begin{aligned}\int_{-\frac{1}{2}}^{\frac{1}{2}} S(f)|P(f)|^2\, df &= \frac{2N_0\beta}{T_b}\int_{-\frac{T_bB_p}{2\beta}}^{\frac{T_bB_p}{2\beta}} |P(f)|^2\, df \\ &= \frac{2N_0L\beta^2}{T_b}.\end{aligned} \tag{B.7}$$

Then, if we define the factor $\alpha = T_bB_p$, the noise power becomes

$$\sum_{i,l=0}^{L\beta} p_i^* \cdot p_l \cdot r_\omega(i-l) = \frac{N_0B_pL\beta^2}{\alpha}. \tag{B.8}$$

We can observe that when the noise is correlated its power increases by a factor $\frac{\beta^2}{\alpha}$ with respect to uncorrelated noise. In fact, even for $\beta = 1$ the noise power increases by $\frac{1}{\alpha}$ since for this sampling rate the noise is slightly correlated. Finally, substituting (B.8) in (B.4), the SNR at the output of the correlator when the noise is correlated is

$$SNR_c = \frac{\alpha(L\beta)^2|A|^2}{N_0B_pL\beta^2} = \alpha L \cdot SNR. \tag{B.9}$$

Since the power of the correlated noise grows exponentially with β, this growth is cancelled with the same exponential growth from the signal power and, consequently, the SNR remains the same. Thus, the resulting SNR_c is always the same as when $\beta = 1$, which explains why the variance plots in the simulation results never go below the CRB. In contrast, because the length of the training sequence does not affect the correlation of the noise, an increase in L will improve the variance.

In the case of the amplitude estimation, we can observe the effect of the correlated noise by calculating the variance of the estimator, which is given by

$$\begin{aligned} \mathrm{var}(\hat{A}) &= \mathbb{E}[\left|\frac{\mathbf{p}^H(\tau_0)\mathbf{x}}{\mathbf{p}^H(\tau_0)\mathbf{p}(\tau_0)} - \mathbb{E}[\hat{A}]\right|^2] = \mathbb{E}[\left|\frac{A\mathbf{p}^H(\tau_0)\mathbf{p}(\tau_0) + \mathbf{p}^H(\tau_0)\boldsymbol{\omega}}{\mathbf{p}^H(\tau_0)\mathbf{p}(\tau_0)}\right|^2] - \mathbb{E}[\hat{A}]^2 \\ &= \frac{\mathbf{p}^H(\tau_0)\mathbf{R}_\omega\mathbf{p}(\tau_0)}{\mathbf{p}^H(\tau_0)\mathbf{p}(\tau_0)} = \frac{\sum_{i,l=0}^{L\beta} p_i^* \cdot p_l \cdot r_\omega(i-l)}{\mathbf{p}^H(\tau_0)\mathbf{p}(\tau_0)} = \frac{L\beta^2 \cdot r_\omega(0)}{\alpha L^2\beta^2} = \frac{2N_0B_p}{\alpha L}, \end{aligned} \tag{B.10}$$

where $\alpha = T_bB_p$. As in the TOA estimation, the variance is not affected by a change in the sampling rate. However, when L is increased the variance of the amplitude estimator is reduced.

Bibliography

[1] FCC Publications. FCC acts to promote competition and public safety in enhanced wireless 911 services. `http://transition.fcc.gov/Bureaus/Wireless/News_Releases/1999/nrwl9040.html`, September 1999.

[2] SS Wang, Marilynn Green, and M Malkawa. E-911 location standards and location commercial services. In *Emerging Technologies Symposium: Broadband, Wireless Internet Access, 2000 IEEE*, pages 5–pp. IEEE, 2000.

[3] 3GPP TS 22.071. *UMTS; LTE; Location Services (LCS) Service description; Stage 1*, ver. 11.0.0 Release 11.

[4] A. Küpper. *Location-Based Services: Fundamentals and Operation.* Wiley, 2005.

[5] Emiliano Trevisani and Andrea Vitaletti. Cell-id location technique, limits and benefits: an experimental study. In *Mobile Computing Systems and Applications, 2004. WMCSA 2004. Sixth IEEE Workshop on*, pages 51–60. IEEE, 2004.

[6] Mahe Zabin and Roja Rani Mannam. Comparative performance analysis of manet routing protocols in internet based mobile ad-hoc networks, 2012.

[7] Camillo Gentile, Nayef Alsindi, Ronald Raulefs, and Carole Teolis. *Geolocation Techniques: Principles and Applications.* Springer, 2012.

[8] Peter Brida, Peter Cepel, and Jan Duha. The accuracy of RSS based positioning in GSM networks. In *Microwaves, Radar & Wireless Communications, 2006. MIKON 2006. International Conference on*, pages 541–544. IEEE, 2006.

[9] 3GPP TS 45.010. *Digital cellular telecommunications system (Phase 2+); Radio subsystem synchronization*, Release 8.

[10] 3GPP TS 45.008. *Digital cellular telecommunications system (Phase 2+); Radio subsystem link control*, Version 11.3.0 Release 11.

[11] Kazuaki Murota and Kenkichi Hirade. GMSK modulation for digital mobile radio telephony. *Communications, IEEE Transactions on*, 29(7):1044–1050, 1981.

[12] 3GPP TS 45.004. *Technical Specification Group GSM/EDGE Radio Access Network; Modulation*, Release 8.

[13] Dayan Adionel Guimarães. Contributions to the Understanding of the MSK Modulation. *Revista Telecomunicações*, 11:1–13, 2008.

[14] EA Norre and MH Jan. GSMsim, A Matlab Implementation of a GSM Simulation Platform. Aalborg University, 1997.

[15] Andrea Goldsmith. *Wireless communications.* Cambridge university press, 2005.

[16] Ling Chen, Marc Loschonsky, and Leonhard M Reindl. Large-Scale Fading Model for Mobile Communications in Disaster and Salvage Scenarios. In *Wireless Communications and Signal Processing (WCSP), 2010 International Conference on*, pages 1–5. IEEE, 2010.

[17] Ling Chen, Marc Loschonsky, and Leonhard M Reindl. Characterization of Delay Spread for Mobile Radio Communications Under Collapsed Buildings. In *Personal Indoor and Mobile Radio Communications (PIMRC), 2010 IEEE 21st International Symposium on*, pages 329–334. IEEE, 2010.

[18] Ling Chen, Marc Loschonsky, and Leonhard M Reindl. Autoregressive Modeling of Mobile Radio Propagation Channel in Building Ruins. *Microwave Theory and Techniques, IEEE Transactions on*, 60(5):1478–1489, 2012.

[19] L. Chen. *Characterization and Modeling of the Mobile Radio Propagation Channel in Disaster Scenarios.* PhD thesis, 2012.

[20] 3GPP TR 45.050. *Digital cellular telecommunications system (Phase 2+);Background for Radio Frequency (RF) requirements*, Version 11.0.0 Release 11.

[21] G. Jacovitti and G. Scarano. Discrete Time Techniques for Time Delay Estimation. *IEEE Transactions on Signal Processing*, 41(2):525–533, 1993.

[22] Josep Vidal, Montse Nájar, and René Játiva. High resolution time-of-arrival detection for wireless positioning systems. In *Vehicular technology conference, 2002. Proceedings. VTC 2002-Fall. 2002 IEEE 56th*, volume 4, pages 2283–2287. IEEE, 2002.